Astronomy & Astrophysics

Chasing ICM cooling and AGN feedback from the macro to the meso scales in the galaxy cluster ZwCl 235

F. Ubertosi[1,2] , M. Gitti[1,3], and F. Brighenti[1,4]

[1] Dipartimento di Fisica e Astronomia, Università di Bologna, Via Gobetti 93/2, 40129 Bologna, Italy
    e-mail: `francesco.ubertosi2@unibo.it`
[2] Istituto Nazionale di Astrofisica (INAF) – Osservatorio di Astrofisica e Scienza dello Spazio (OAS), Via Gobetti 101, 40129 Bologna, Italy
[3] Istituto Nazionale di Astrofisica (INAF) – Istituto di Radioastronomia (IRA), Via Gobetti 101, 40129 Bologna, Italy
[4] University of California Observatories/Lick Observatory, Department of Astronomy and Astrophysics, University of California, Santa Cruz, CA 95064, USA

ABSTRACT

Aims. We aim to investigate the interplay between the intracluster medium (ICM) and the active galactic nucleus (AGN) in ZwCl 235, a galaxy cluster with high X-ray flux, an extended central radio galaxy, and evidence of multiphase gas at its center.
Methods. Using archival data from the *Chandra* telescope, the Very Large Array Sky Survey (VLASS), the LOFAR Two-metre Sky Survey (LOTSS), and the VLBA telescope, we performed a complete study of ZwCl 235, dissecting the dynamics of the ICM, the thermodynamic state of the central gas, and the properties of the brightest cluster galaxy (BCG). By means of radial profiles and 2D spectral maps, we measured the temperature, entropy, and cooling time of the ICM, and we compared the morphology of the central radio galaxy with the surrounding medium.
Results. We find evidence that ZwCl 235 is a sloshing cool core cluster in which the activity of the central galaxy has excavated a pair of cavities and possibly uplifted enriched gas to an altitude of ~30 kpc. In the cluster core, the lowest entropy ICM is preferentially found in a 20 kpc-long filament tangential to the southern radio lobe of the AGN. We argue that the observed cool (~1.3 keV) filament is likely produced by a combination of sloshing and stimulated ICM cooling, which may be fueling the central supermassive black hole. Additionally, we determined that the X-ray emission of the BCG originates from a ~1.4 keV plasma kernel, which extends for 5 kpc in radius and has a short cooling time (~240 Myr), and it could represent the thermal corona of the BCG.
Conclusions. Overall, we propose that several sources (the large-scale ICM, the low entropy filament, and the ~1.4 keV kernel) of cold material are currently feeding the central AGN, and that the ICM cooling cycle expectations are met from the macro scales (between 5−100 kpc) to the meso scales (≤5 kpc) of AGN feedback.

Key words. galaxies: clusters: intracluster medium – X-rays: galaxies: clusters – radio continuum: galaxies – galaxies: active

1. Introduction

The cores of galaxy clusters represent the region where the interplay between different cluster components – namely the intracluster medium (ICM), the brightest cluster galaxy (BCG), and the central active galactic nucleus (AGN) – is manifested (e.g., for reviews McNamara & Nulsen 2007, 2012; Gitti et al. 2012; Morganti 2017; Combes 2017; Gaspari et al. 2020; Eckert et al. 2021). In particular, the investigation of "cool core" galaxy clusters (see e.g., Molendi & Pizzolato 2001; Hudson et al. 2010; Bharadwaj et al. 2014 for a discussion of cool core systems) with a multiwavelength approach has recently allowed for new light to be shed on how AGN accretion and ejection mechanisms are coupled with the thermodynamic properties of the surrounding ICM (for recent works see e.g., Rose et al. 2019a,b; Vantyghem et al. 2019; Ciocan et al. 2021; Mohapatra et al. 2022; McKinley et al. 2022; Temi et al. 2022).

The high resolution *Chandra* and *XMM-Newton* X-ray observations of these objects have led to measurements of the central gas temperature and density, finding that cooling of the ICM can lead to cold gas (~1 keV) reservoirs around the BCG (e.g., Peterson et al. 2001; Donahue & Voit 2004;

Peterson & Fabian 2006), albeit lower than predicted from the standard cooling flow model of Fabian (1994). Imaging of the cluster cores revealed surface brightness depressions called X-ray cavities, which were found to be coincident with the lobes of the radio galaxy hosted in the BCG (see e.g., Boehringer et al. 1993; Churazov et al. 2000; McNamara et al. 2000; Fabian et al. 2000; Bîrzan et al. 2004). These works showed that the energy required to excavate the bubbles (in the range 10^{55-62} erg, e.g., van Weeren et al. 2014; Hlavacek-Larrondo et al. 2015; Shin et al. 2016) matches the energy released by cooling of the ICM; these pieces of evidence suggest that cluster central AGNs can prompt a deposition of energy in the ICM, preventing an over-cooling of the same gas that fuels their supermassive black holes (SMBHs; e.g., McNamara & Nulsen 2007, 2012). This finely tuned balance is usually referred to as the AGN feedback cycle.

The end product of ICM cooling is predicted to form reservoirs of multiphase gas surrounding the BCG. Warm gas (~10^4 K) glowing in line emission (e.g., Hα, see e.g., McDonald et al. 2010; Hamer et al. 2016) and molecular gas detected in CO (~10−100 K, see e.g., Edge 2001; Combes 2018; Russell et al. 2019) have been found to be cospatial with the

lowest entropy ICM. The multitemperature medium is usually filamentary and is thought to generate from condensation of the hot cluster gas (e.g., McDonald et al. 2010; Gaspari et al. 2020). Furthermore, several combined X-ray, radio as well as optical and millimeter studies have discovered that the cold filaments are draped around or trail X-ray cavities (e.g., Hamer et al. 2012; McDonald et al. 2015; Olivares et al. 2019; Rose et al. 2019b). This coincidence has led to theories that the link between AGN activity and ICM cooling consists not only in lowering the amount of fuel, but also in setting the conditions for condensation to occur (e.g., Brighenti et al. 2015; Yang & Reynolds 2016). In addition to heating the surrounding medium, the expansion and rise of X-ray cavities can drag enriched, cold material from the central regions up to several tens of kiloparsecs (e.g., Gitti et al. 2011). By lifting low temperature gas to an altitude where cooling times and dynamical times become competitive, the condensation of the ICM into warm and cold gas kernels is stimulated (e.g., Gaspari & Sądowski 2017).

In this context, it is interesting to note that in roughly two-thirds of cool core clusters, there are surface brightness edges (named "cold fronts") wrapped around the center in a spiral morphology (Ghizzardi et al. 2010; Zuhone & Roediger 2016). Additionally, these system can show spatial offsets between the BCG and the coldest phase of the ICM. The mechanism generating these features is sloshing of the gas in the potential well of the cluster, triggered by gravitational perturbations of the system (for reviews see Markevitch & Vikhlinin 2007; ZuHone et al. 2013; Zuhone & Roediger 2016); the oscillation of the cold gas leads to the formation of cold fronts on a large scale, and it can separate the peak of ICM emission from the AGN in the central regions. Recent studies have shown that sloshing can be responsible for offsetting not only the hot ICM ($T \sim 10^{7-8}$ K), but also the multiphase gas surrounding the BCG (e.g., Combes 2018; Pulido et al. 2018; Vantyghem et al. 2019), generating asymmetries in the distribution of the warm ($T \sim 10^4$ K) and cold ($T \sim 10-100$ K) phases. As this component is believed to sustain the activity of the central AGN by feeding the SMBH, a recent interest in the effect of sloshing on the feedback cycle has been growing. If sloshing separates the AGN and its fuel reservoirs, then the stability of feeding and feedback might be affected. Early results suggest that sloshing does not break the feedback cycle, but it could possibly influence the timescales of AGN activity (as in e.g., Abell 1991, Hamer et al. 2012; Abell 2495, Pasini et al. 2019; Abell 1668, Pasini et al. 2021).

2. The galaxy cluster ZwCl 235

To explore which conditions trigger the formation of a multiphase medium around BCGs and how the dynamics of the environment can influence AGN feeding and feedback, systems with a relatively high X-ray flux and bright in Hα (suggesting the presence of cool gas) can be considered. To identify a potentially interesting system, we selected objects with an X-ray flux greater than 9.0×10^{-12} erg cm^{-2} s^{-1} from the BCS survey of Ebeling et al. (1998), and with an Hα luminosity greater than 10^{40} erg s^{-1} from the sample of Crawford et al. (1999) (for a similar selection see Ettori et al. 2013; Pasini et al. 2019, 2021). The 18 objects satisfying these criteria are listed in Table 1. Many clusters in the list (e.g., Abell 2052, 2A0335+096, Abell 1835, Abell 1795, Abell 1991, and Abell 2199) provide archetypal examples of the interplay between the central AGN and the surrounding gas for the detection of X-ray cavities, for the existence of filamentary warm nebulae, and/or for the effect of sloshing on the central cool gas. Other objects, such as Abell 2495 and

Abell 1668 (characterized by a relatively low Hα luminosity, see Table 1), have been investigated only recently: the analysis of the two revealed evidence for a sloshing-influenced AGN feedback cycle – with these clusters having the X-ray peak, the BCG, and the warm Hα-emitting gas phase offset from each other (Pasini et al. 2019, 2021). As an informative remark, we note that a similar X-ray flux selection in, for example, the REFLEX sample (Böhringer et al. 2004a) identifies other objects (e.g., S1101, Hydra A, Abell 85, Abell 133, Abell 496, Abell 2597, NGC 5044, and Centaurus) that represent further notable laboratories where the AGN-ICM interplay has been extensively investigated.

In this work we progress on the study of X-ray and Hα bright systems by focusing on ZwCl 235, one of the two clusters in Table 1 that still lacks a dedicated study (the other being Abell 2009). ZwCl 235 is a nearby system ($z \sim 0.083$) located at RA, Dec = 00:43:52.0, +24:24:21 (J2000), with $f_X = 1.1 \times 10^{-11}$ erg cm^{-2} s^{-1}, $L_X^{0.1-2.4\,\mathrm{keV}} = 3.22 \times 10^{44}$ erg s^{-1}, and $L_{H\alpha} = (4.1 \pm 0.6) \times 10^{40}$ erg s^{-1}. The cluster has a 20 ks observation in the *Chandra* data archive[1] that allows us to investigate the ICM properties. However, the high spatial resolution multiwavelength coverage of ZwCl 235 is scarce (compared to the well-studied objects at the top of Table 1). This source is twelfth in Hα luminosity in the list of 18 sources, indicating a relatively low star formation rate. This is consistent with the submillimeter IRAM observations presented in Salomé & Combes (2003), which found hints of CO(1−0) line emission in the core of ZwCl 235 and failed to detect CO(2−1), thus placing an upper limit on the molecular mass of $M_{\mathrm{mol}} \leq 2.5 \times 10^9 \, M_{\odot}$ (in the same work, molecular masses of more than $4 \times 10^{10} \, M_{\odot}$ were measured in Abell 1068 and Abell 1795). The relatively low level of star formation is also evident from the upper limit on the infrared luminosity set by Quillen et al. (2008), a feature shared with Abell 2009, Abell 1668, Abell 2495, and Abell 1991, that is to say the systems in Table 1 have an Hα luminosity similar to or below that of ZwCl 235. The radio emission of the BCG in ZwCl 235 between 1 GHz−150 GHz was analyzed in Hogan et al. (2015a,b), who found that a single power law of flat spectral index $\alpha = -0.45$ provides a good description of the radio spectral energy distribution, indicating a core-dominated source. Faint and extended – but barely resolved – radio lobes connected to the bright core are visible in the survey LOFAR image at 144 MHz shown in Bîrzan et al. (2020). Since dedicated, spatially resolved radio observations of the AGN in ZwCl 235 are missing, we employed survey radio images to further examine the radio morphology of the BCG. Overall, our aim is to investigate the X-ray and radio properties of ZwCl 235 and to discuss the results in light of the optical and submillimeter information mentioned above, in order to draw a picture of AGN feeding and feedback in this system.

This paper is organized as follows: Section 3 describes the radio and X-ray data used in this work, summarizing the main steps of data reduction. The analysis and results are reported in Sect. 4, with dedicated subsections to present, in particular, the radio properties of the BCG (Sect. 4.1), the general X-ray analysis of the cluster (Sects. 4.2 and 4.3), the radio and X-ray evidence for AGN feedback (Sect. 4.4), the peculiarities of the metal distribution in the ICM (Sect. 4.5), the X-ray emission from the BCG (Sect. 4.6), and the properties of the ICM in the central 15 kpc (Sect. 4.7). We discuss our results in Sect. 5, and summarize our main conclusions in Sect. 6.

---

[1] https://cxc.harvard.edu/cda/

Table 1. Systems with X-ray flux greater than 9×10^{-12} erg cm^{-2} s^{-1} from the sample of Ebeling et al. (1998), and with an Hα luminosity greater than 10^{40} erg s^{-1} from the sample of Crawford et al. (1999), ordered by decreasing Hα luminosity.

Object	f_X [erg cm^{-2} s^{-1}]	$L_{H\alpha}$ [erg s^{-1}]	Literature (e.g.)
Abell 1068	9.4×10^{-12}	172.3×10^{40}	(1), (2)
Abell 1835	14.7×10^{-12}	163.9×10^{40}	(3), (4)
Abell 2204	21.9×10^{-12}	159.4×10^{40}	(5), (6)
Abell 2390	9.6×10^{-12}	61.6×10^{40}	(7), (8)
RXJ1720+26	14.3×10^{-12}	12.7×10^{40}	(9)
Abell 115	9.0×10^{-12}	12.7×10^{40}	(10)
ZwCl 8276	16.4×10^{-12}	12.5×10^{40}	(11)
Abell 1795	68.1×10^{-12}	11.3×10^{40}	(12), (13)
Abell 478	39.9×10^{-12}	10.8×10^{40}	(14)
2A0335+096	80.5×10^{-12}	10.3×10^{40}	(15), (16)
Abell 2009	9.2×10^{-12}	6.1×10^{40}	(...)
ZwCl 235	10.9×10^{-12}	4.1×10^{40}	(...)
Abell 2199	96.8×10^{-12}	2.7×10^{40}	(17)
Abell 2052	47.1×10^{-12}	2.6×10^{40}	(18), (19)
Abell 1668	9.3×10^{-12}	2.3×10^{40}	(20)
Abell 2495	11.8×10^{-12}	2.0×10^{40}	(21)
Abell 2634	23.1×10^{-12}	1.3×10^{40}	(22), (23)
Abell 1991	9.4×10^{-12}	1.1×10^{40}	(24), (25)

Notes. The target of our study (ZwCl 235) is highlighted in red. (1) Object name; (2) X-ray flux; (3) Hα luminosity; (4) Examples of relevant literature studies dedicated to the object: (1) McNamara et al. (2004); (2) Wise et al. (2004); (3) McNamara et al. (2006); (4) McNamara et al. (2014); (5) Sanders et al. (2009a); (6) Chen et al. (2017); (7) Allen et al. (2001); (8) Sonkamble et al. (2015); (9) Mazzotta et al. (2001); (10) Hallman et al. (2018); (11) Ettori et al. (2013); (12) Kokotanekov et al. (2018); (13) Russell et al. (2017); (14) Sun et al. (2003); (15) Sanders et al. (2009b); (16) Vantyghem et al. (2016); (17) Nulsen et al. (2013); (18) Blanton et al. (2011); (19) Balmaverde et al. (2018); (20) Pasini et al. (2021); (21) Pasini et al. (2019); (22) Schindler & Prieto (1997); (23) Sun et al. (2007); (24) Sharma et al. (2004); and (25) Hamer et al. (2012).

We adopt the following cosmology: $H_0 = 70$ km s^{-1} Mpc^{-1}, $\Omega_m = 0.3$, and $\Omega_\Lambda = 0.7$, which results in a conversion between linear and angular scales of 1.56 kpc/$''$ at the redshift of ZwCl 235 (corresponding to a luminosity distance of $D_L = 378$ Mpc). We report every uncertainty at the 1σ confidence level. The radio spectral index α is defined as $S_\nu \propto \nu^\alpha$ (where ν is the frequency and S_ν is the flux density).

3. Data and methods

3.1. Radio data – LOFAR, VLA, VLBA

A primary aim of this work is to derive the properties of the central radio galaxy and perform comparisons with the X-ray observation. To this end, we employed radio observations at different frequencies and with different resolutions.

LOFAR – 144 MHz. The recent release of the LOFAR Two-meter sky survey DR2 (Shimwell et al. 2022) allows us to access the LOFAR observation of ZwCl 235, originally published in Bîrzan et al. (2020). The 144 MHz total intensity image has been retrieved from the archive[2] and is shown in Fig. 1. The resolution is $6'' \times 6''$, and the rms noise is $\sigma_{rms} = 0.1$ mJy beam^{-1}.

---

[2] https://lofar-surveys.org/dr2_release.html

VLA – 3 GHz. ZwCl 235 has also been observed as part of the VLA Sky Survey at 3 GHz. The observation is part of the second campaign of the first survey epoch (VLASS1.2, Lacy et al. 2020), and the target falls in the tile T17t01. The 3 GHz total intensity image has been retrieved from the archive[3] and is shown in Fig. 1. The resolution is $2.7'' \times 2.5''$ (position angle PA = 162°), and the rms noise is $\sigma_{rms} = 0.2$ mJy beam^{-1}. The fluxes (within $3\sigma_{rms}$) of the different components have been measured in CASA 6.1.2 (see Sect. 4.1).

VLBA – 5 GHz. The source has been targeted with the VLBA at 5 GHz in phase-referencing mode for 45 min. Hogan et al. (2015b) reported that at milli-arcsecond (mas) scale the source is extended, showing a two-sided jet structure. In order to perform morphological comparisons with the VLA data, we obtained the VLBA data at 5 GHz from the archive[4]. Standard data reduction was performed in AIPS v.31DEC20. The VLBA data were imaged in AIPS using the task IMAGR and setting the robust parameter to 1, obtaining total and peak flux measurements consistent with those of Hogan et al. (2015b). The resulting radio map, at a resolution of 3.2×1.3 mas (rms noise $\sigma_{rms} = 26$ μJy beam^{-1}), is shown in Fig. 1.

3.2. X-ray data – Chandra

ZwCl 235 was observed by *Chandra* using ACIS-S during Cycle 11 (ObsID 11735), for a total, uncleaned exposure of 19.8 ks. We retrieved the data from the *Chandra* archive[5] and reprocessed the observation using CIAO-4.13. Point sources were identified using the tool wavdetect, and masked during the morphological and spectral analysis. By cross-matching the detected X-ray point sources with the USNO-A.2 optical catalog we verified that the astrometry of the *Chandra* observation does not need further corrections beyond its nominal pointing accuracy (0.4$''$). We filtered the data from periods contaminated by background flares, obtaining a cleaned exposure of 19.5 ks. The blank-sky event file matching the observation of ZwCl 235 has been selected as background file, and normalized by the 9−12 keV count-rate of the observation.

In order to investigate in details the morphology of the ICM, we produced images and corresponding background and exposure maps in the 0.5−7 keV energy band. These images have been used to extract surface brightness profiles, which were fit using the software Proffit-1.5 (Eckert et al. 2011).

Spectral fitting has been performed in the 0.5−7 keV band using XSPEC v.12.10, binning the spectra to 25 cts per bin and applying the χ-statistics (unless otherwise stated). For every model discussed in this article, we employed the table of solar abundances of Asplund et al. (2009). When fitting the spectra, we always included an absorption model (tbabs) to account for Galactic absorption, with the column density fixed at the value $N_H = 3.57 \times 10^{20}$ cm^{-2} (HI4PI Collaboration 2016). When included in the fitting model, the redshift $z = 0.083$ was also fixed.
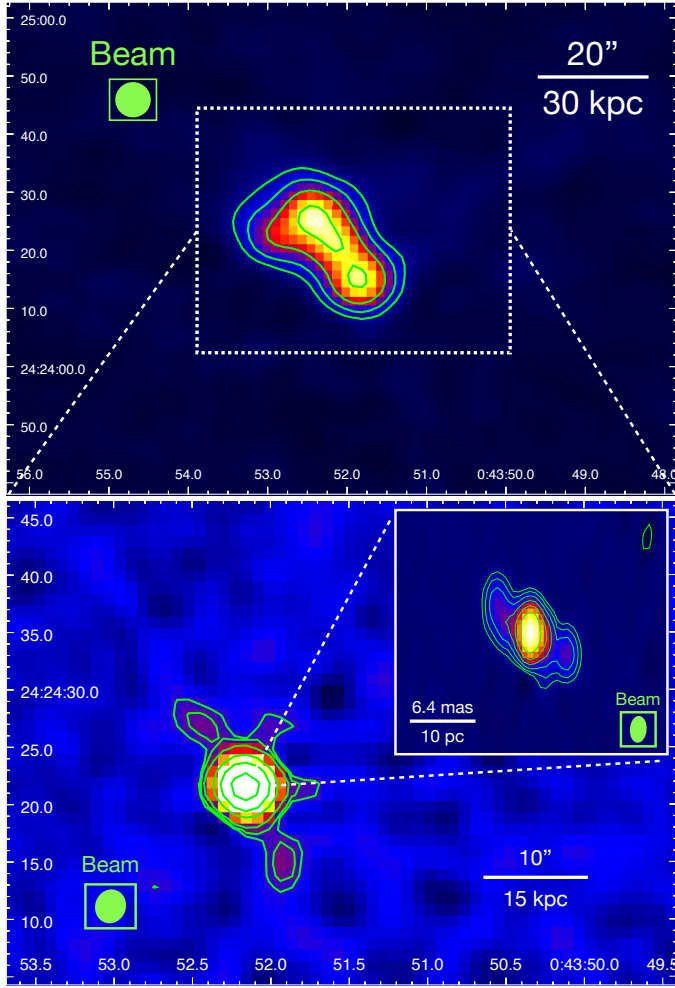
4. Results

In the following we describe the results of the morphological and spectral analysis of the radio and X-ray data of ZwCl 235 and of the central AGN.

---

[3] science.nrao.edu/vlass/data-access
[4] https://data.nrao.edu
[5] cda.harvard.edu/chaser

Fig. 1. Resolved radio observations of ZwCl 235. *Upper panel*: 144 MHz LOTSS DR2 image of ZwCl 235, at a resolution of 6″. Green contours are drawn at 5, 10, 20, 40 × σ_{rms} (with σ_{rms} = 0.1 mJy beam^{-1}). *Lower panel*: 3 GHz VLASS image of the radio galaxy in the BCG, at a resolution of 2.7″ × 2.5″. Green contours are drawn at 3, 6, 12, 36, 72, 144, 288 × σ_{rms} (with σ_{rms} = 0.2 mJy beam^{-1}). *Lower zoom-in*: 5 GHz VLBA image of the core, at a resolution of 3.2×1.3 mas. Green contours are drawn at 4, 8, 16, 32, 64, 128 × σ_{rms} (with σ_{rms} = 26 μJy beam^{-1}). For each panel, the beam is represented by a green circle.

4.1. The central radio galaxy

In this section we discuss the morphology and spectral properties of the radio galaxy associated with the BCG of ZwCl 235, combining our new results with those presented in the literature.

In the upper panel of Fig. 1 we show the 144 MHz LOFAR observation of the cluster, that reveals extended radio lobes (each ~20 kpc long) oriented northeast (NE) to southwest (SW), with a position angle of ~130°. Using this observation, Bîrzan et al. (2020) measured the source total flux density $S_\nu = 151 \pm 24$ mJy.

The lower panel of Fig. 1 shows the VLASS 3 GHz image of the radio galaxy at the center of ZwCl 235. The morphology is slightly resolved, showing a bright core, two opposite radio lobes extending NE to SW for roughly 15 kpc, and two small west protrusions. The source has a total flux density of 37.7 ± 1.0 mJy, with a contribution of 32 ± 0.9 mJy coming from the bright core (which supports the result of Hogan et al. 2015b that the total flux of this radio galaxy is dominated by the core emission). We note the similar morphology between the 3 GHz image and the

144 MHz one, as both unveil the presence of radio lobes with a position angle of ~130°.

Exploring radio emission on the parsec scale can provide further insights on the AGN activity of a BCG (e.g., Liuzzo et al. 2010). To this end, in the zoom-in of Fig. 1 we show the VLBA 5 GHz image of the radio galaxy's core at a resolution of 3.1 × 1.4 mas² (~4.7 × 2.1 parsec²). We recover an unresolved core plus a two sided-jet structure oriented NE to SW (consistent with Hogan et al. 2015b). Each jet has a projected length of ≈10 pc. The position angles of the jets, measured with a straight line passing through the core that connects the two jets, is ~140°, which is in good agreement with that of the radio galaxy on kiloparsec scale. Therefore, the VLBA image likely unveils the details of the jets that have inflated the radio lobes seen at 3 GHz and 144 MHz. Moreover, the bright core visible in the VLBA data indicates that the central engine of the BCG is currently active (consistent with the aforementioned core dominance). By placing the core radio properties of ZwCl 235 in the context of other BCGs, we can specifically determine how active the source is with respect to the general population. In particular, we refer to the results of Hogan et al. (2015b), who determined from the radio spectrum that the core component of this radio galaxy is expected to have a radio power of roughly 4×10^{23} W Hz^{-1} at 10 GHz, and put an upper limit to the expected radio power at 1 GHz of any extended emission of ≤1.2×10^{24} W Hz^{-1}. On the one hand, the 10 GHz core radio power places ZwCl 235 in the top 20% of the sample of Hogan et al. (2015b), which indicates that the central AGN is currently more active than most other BCGs. On the other hand, the upper limit on the 1 GHz radio power of extended components is close to the average of the sample, suggesting that on longer timescales the activity of the central radio galaxy is typical of BCGs. In this respect, restricting the comparison to the X-ray flux-limited list of Table 1, ZwCl 235 is similar to ZwCl 8276, another core dominated source (see Hogan et al. 2015a,b).

The availability of the LOFAR and VLASS data, that reveal extended lobes of the radio galaxy previously unknown, enables us to constrain the spectral properties of the extended emission by considering the relative contribution of the core flux to the total flux. Using an archival, snapshot VLA observation at 4.8 GHz of ZwCl 235 (which did not resolve the source, having a beam of ~5″ FWHM), Hogan et al. (2015b) measured a total flux of 30.3 mJy and a core peak flux of 27.3 mJy (88% of which is recovered by the VLBA observation, see Hogan et al. 2015b). Combining these information at 4.8 GHz with our measurements at 3 GHz and the total flux measured by LOFAR at 144 MHz, we estimate the spectral index of the core and extended components of the radio galaxy with the following methods:

Unresolved core. The 32 mJy at 3 GHz from the VLASS data and 27.3 mJy at 4.8 GHz from the VLA data suggest a core spectral index of $\alpha_3^{4.8} \approx -0.3$. This rather flat value is in good agreement with the expected emission from a core: in Hogan et al. (2015b) the average core spectral index of BCGs is −0.33; limiting ourselves to the sources listed in Table 1 we find $\overline{\alpha} = -0.31$.

Extended components at GHz frequencies. The subtraction of the core flux from the total flux can provide an estimate of the amount of emission coming from extended components. With residual fluxes of 5.7 mJy at 3 GHz and 3 mJy at 4.8 GHz, the extended component spectral index measured from the VLA and VLASS data is $\alpha_3^{4.8} \approx -1.3$. A steep spectral index ($\alpha \leq -1$) is usually associated with the aging of the electron population responsible for the radio emission.

Extended components between MHz and GHz frequencies. Following the procedure described in Ubertosi et al. (2021), we estimated the relative contribution of the core and the extended components to the total flux at 144 MHz (≈ 151 mJy, Bîrzan et al. 2020). Assuming that the core spectral index remains flat at lower frequencies, we extrapolated the AGN flux at 3 GHz to 144 MHz, finding $S_{\text{core}}^{144\,\text{MHz}} \approx 73$ mJy and thus $S_{\text{extended}}^{144\,\text{MHz}} = S_{\text{total}}^{144\,\text{MHz}} - S_{\text{core}}^{144\,\text{MHz}} \approx 78$ mJy. This corresponds to a 144 MHz–3 GHz spectral index of the extended components of $\alpha_{0.144}^{3} \approx -0.87$.

Overall, our estimates support a steepening beyond 3 GHz of the spectral index of the extended components detected by the VLASS and the VLA. Instead, regarding the core emission, Hogan et al. (2015a) reported a possible steepening of the spectrum only beyond 100 GHz (with fluxes at 16 GHz, 90 GHz and 150 GHz of 16.7 mJy, 9.9 mJy and 4.7 mJy, respectively). We note that our estimates above for the extended components should be treated with caution, as a proper measurement of the spectral index would require observations with similar $u-v$ coverage, or at least to resolve the same structures. If confirmed by future, more sensitive and resolved radio observations, the above results would be consistent with aging of the radio lobes. Using the available data and adopting a few assumptions, it is possible to derive only a tentative upper limit on the radiative age of the lobes. In particular, given the spectral break frequency ν_b [GHz] and the magnetic field of the radio galaxy B [μG], it is possible to obtain the radiative age of a synchrotron emitting source (e.g., Eilek 2014):

$$\tau_{\text{syn}}[\text{Myr}] = 1590 \frac{B^{1/2}}{B^2 + B_{\text{IC}}^2} [\nu_{\text{br}}(1 + z)]^{-1/2} \quad (1)$$

where $B_{\text{IC}} = 3.2(1 + z)^2$ μG is the cosmic microwave background equivalent magnetic field. Due to the steepening of the spectral index of extended emission on the VLA-LOFAR kiloparsec scales beyond 3 GHz, we can assume $\nu_{\text{br}} = 3$ GHz. Since the flux of extended components from the snapshot VLA observation at 4.8 GHz is likely to be a lower limit, it is possible that the break frequency could be higher than 3 GHz. Therefore, the derived τ_{syn} has to be treated as an upper limit. In light of this consideration, we used the minimum energy loss field $B = B_{\text{IC}}/\sqrt{3} = 2.17$ μG (see de Gasperin et al. 2017), that minimizes the radiative losses of the emitting particles. This second assumption provides another upper limit on the radiative lifetime, thus it is consistent with selecting $\nu_{\text{br}} = 3$ GHz. By substituting these values in Eq. (1) we obtained $\tau_{\text{syn}} \lessapprox 70$ Myr.

4.2. Global X-ray properties of the ICM: Radial profiles and spectral maps

We show in Fig. 2 (left panel) the 0.5−7 keV *Chandra* image of ZwCl 235. The cluster is fairly spherical, with a bright edge to the east of the core. The zoom-in of Fig. 2 (right upper panel) shows a detail of the cluster core, where it is possible to see the X-ray peak coinciding with the center of the BCG (green cross). We note the presence of a bright arm-like feature that, starting from the X-ray peak, bends southeast (SE) and reaches a distance from the center of 15″ (∼23 kpc).

We extracted an azimuthally averaged surface brightness profile from circular annuli with 1″ (∼1.6 kpc) of bin width, extending from 3″ (to avoid any contamination from possible nonthermal X-ray emission related to the central AGN – see

Sect. 4.6 for the analysis of the inner 3″) to 180″ (∼280 kpc) from the center (shown in Fig. 2, right lower panel). The profile is typical of cool core galaxy clusters, as we observe no internal flattening of the profile, but rather a continuous increase in surface brightness toward the center. The profile has been fit with a single β model and a double β model (with a common β value). We found that the double β model with a χ/d.o.f. = 195/166 provides a better description of the surface brightness profile with regard to the single β model, with a χ/d.o.f. = 205/168 (F statistics value of 4.3, p value of 0.016). This is typical of cool core galaxy clusters displaying an excess surface brightness with regard to the single β model (e.g., Mohr et al. 1999). The best fit parameters are $\beta = 0.54 \pm 0.02$, inner core radius $r_1 = 11.4″ \pm 0.7″$ (17.8 ± 1.1 kpc), outer core radius $r_2 = 53.4″ \pm 9.0″$ (84.9 ± 14.0 kpc), normalization $S_1 = (4.02 \pm 0.13) \times 10^{-3}$ cts s^{-1} arcmin^{-2}, and a ratio $S_2/S_1 = 0.03$.

In order to study the thermodynamic properties of the cluster, we extracted the spectra of circular, concentric annuli centered on the BCG, starting from 3″ from the center to 180″ from the BCG. These annuli were chosen to contain at least 2000 counts, or a signal-to-noise ratio (S/N) of 40. The spectra were fit with a `projct*tbabs*apec` model, leaving the temperature, the metallicity and the normalization free to vary. A deprojected spectral analysis allows to obtain 3D estimates of thermodynamic quantities. In particular, assuming $n_e = 1.2 n_p$, the electron density of the ICM can be derived from the normalization (norm) of the deprojected `apec` component using the following expression (e.g., Gitti et al. 2012):

$$n_e = \sqrt{10^{14}\left(\frac{4\pi \times \text{norm} \times [D_A(1 + z)]^2}{0.83\,V}\right)}, \quad (2)$$

where D_A is the angular distance from the source and V is the projected volume of the emitting region.

From the electron density and temperature of the ICM, we obtained the pressure p, the entropy K, and the cooling time t_{cool} of the ICM defined as

$$p = 1.83\, n_e\, kT \quad (3)$$

$$K = \frac{kT}{n_e^{2/3}} \quad (4)$$

$$t_{\text{cool}} = \frac{\gamma}{\gamma - 1} \frac{kT}{\mu\, X\, n_e\, \Lambda(T)}, \quad (5)$$

respectively, where $\gamma = 5/3$ is the adiabatic index, $\mu \approx 0.6$ is the molecular weight, $X \approx 0.7$ is the hydrogen mass fraction and $\Lambda(T)$ is the cooling function (Sutherland & Dopita 1993). Figure 3 shows deprojected temperature, density, abundance, pressure, entropy and cooling time profiles.

Additionally, we generated spectral maps by binning the 0.5−7 keV image with the CONTOUR BINNING technique (Sanders 2006), in order to obtain a list of regions with a $S/N \geq 30$. Then, we extracted and fitted the spectrum of each region with a thermal model (`tbabs*apec`), and produced maps of best fit values for temperature, metallicity and normalization. From the temperature and normalization maps it is possible to obtain pseudo-pressure (pp), pseudo-entropy (pK) and pseudo-cooling time maps (pt_{cool}). In particular, the emission measure (EM) of the plasma is proportional to the ratio between the `apec` normalization and the number of pixels in each spectral region (norm/n_{pix}). Considering that the electron density is
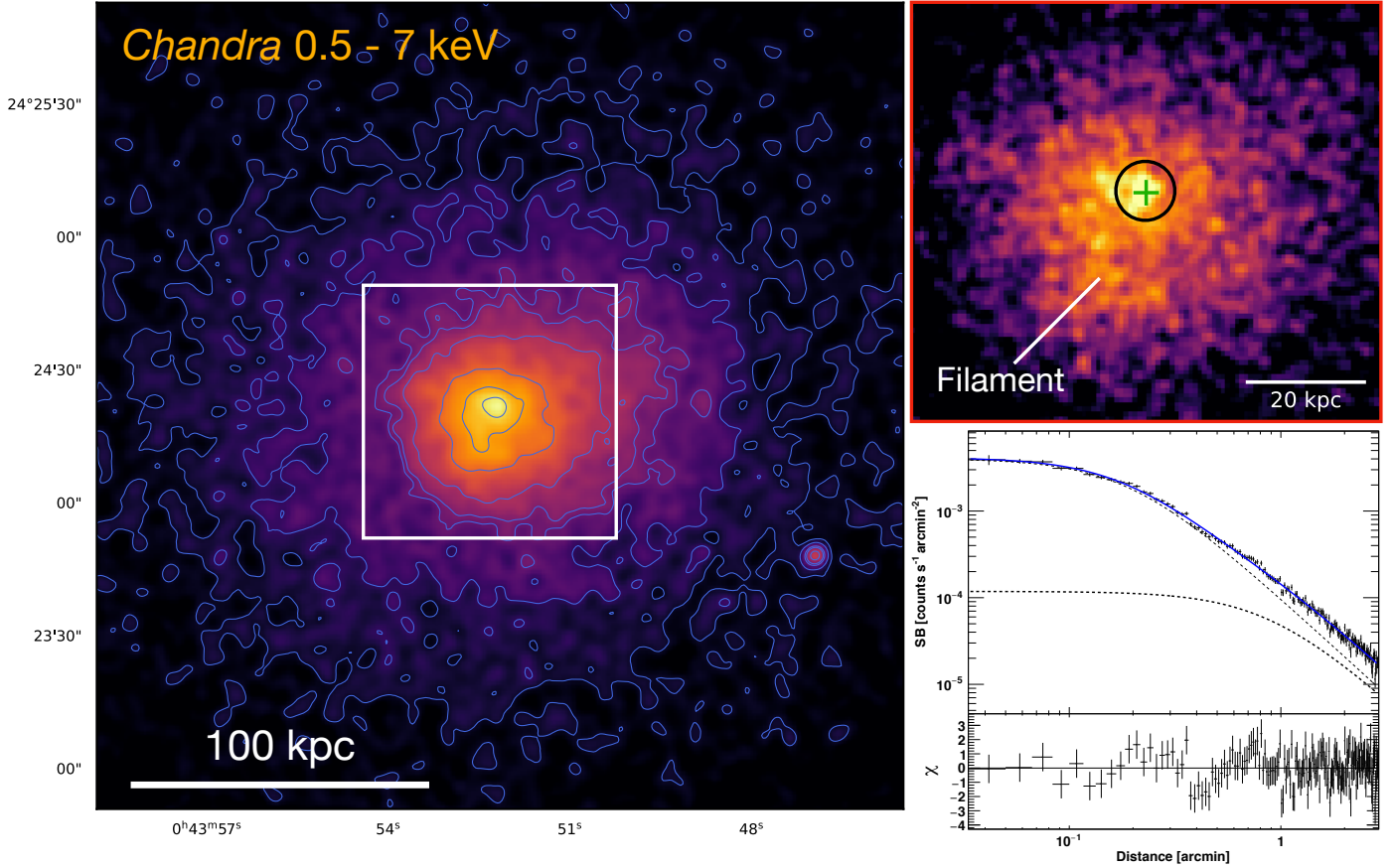
Fig. 2. *Chandra* view of ZwCl 235. *Left panel*: 0.5−7 keV band background subtracted, exposure corrected *Chandra* image of ZwCl 235, centered on the BCG. The image is smoothed with a Gaussian of kernel size 3″. Blue contours are spaced by a factor of 1.5, with the highest being 6×10^{-7} cts s^{-1} cm^{-2}. The white box indicates the size of the zoom-in on the right. *Right upper panel*: zoom-in of the *Chandra* image in the *left panel*, smoothed with a Gaussian of kernel size 1.5″. The green cross marks the BCG center, and the black circle shows the size of the region excised from the surface brightness radial profile. The position of the bright filament discussed in Sects. 4.2 and 4.7 is indicated. *Right lower panel*: surface brightness profile of ZwCl 235, with the best fit double β model overplot with a blue line (dotted black lines represent the contributions of the two β models). The residuals are shown in the lower box.

proportional to the root of the projected emission measure, the above pseudo-maps can be built using the following equations, respectively:

$$pp = kT \times EM^{1/2} \tag{6}$$

$$pK = kT \times EM^{-1/3} \tag{7}$$

$$pt_{\text{cool}} = kT^{1/2} \times EM^{1/2}. \tag{8}$$

We show the kT, pp, pK and pt_{cool} maps in Fig. 4.

As a note of caution, we observe that in order to securely detect spectral features (especially metallicity) from thermodynamic maps, a $S/N \geq 50$ is typically required (e.g., O'Sullivan et al. 2019). However, given the short exposure of the *Chandra* observation of ZwCl 235, we reduced the minimum S/N to 30, in order to preserve good spatial resolution. This resulted in relative uncertainties that can reach ∼20% on temperature and ∼30% on metallicity. Therefore, every feature we tentatively identified from the maps has been subsequently studied in details by extracting and fitting the spectrum of larger regions encompassing the specific feature, thus reaching a higher S/N and more robust results. We note that both the profiles and spectral maps are typical of cool core galaxy clusters, showing a central increase in gas density and a decline in temperature.

It has been argued that the use of `projct` to deproject spectra may generate unphysical oscillating temperature profiles (Russell et al. 2008). As a sanity check, we tested the alternative use of the `dsdeproj` code by Sanders & Russell (2016) to deproject the spectra, which returned consistent results with those of `projct`.

The standard method to determine the magnitude of cooling in a cool core galaxy cluster consists in measuring the bolometric X-ray luminosity associated with the ICM within the so-called cooling radius. It is possible to define the cooling radius as the region within which the cooling time is less than the look-back time at $z = 1$ (roughly 7.7 Gyr; e.g., Bîrzan et al. 2004; Gitti et al. 2012). By fitting the cooling time profile of ZwCl 235 with a power law (see Fig. 3), and locating the intersection with $t_{\text{cool}} = 7.7$ Gyr we measured $r_{\text{cool}} = 78.5 \pm 1.4$ kpc. Then we extracted two spectra, one from the cooling region using an annulus centered on the BCG with inner radius 3″ and outer radius $r_{\text{out}} = r_{\text{cool}}$, and the other extending from r_{cool} to the edge of the chip to account for the ICM projected along the line of sight. The spectra were fitted with a `projct*tbabs*apec` model, which allowed us to measure the properties of the ICM within r_{cool}: we found a temperature $kT = 2.74^{+0.06}_{-0.05}$ keV, a metallicity $Z = 1.21 \pm 0.34$ and an electron density $n_{\text{e}} = (2.8 \pm 0.1) \times 10^{-2}$ cm^{-3} (with χ/d.o.f. = 274/265). The bolometric luminosity of the cooling region was measured
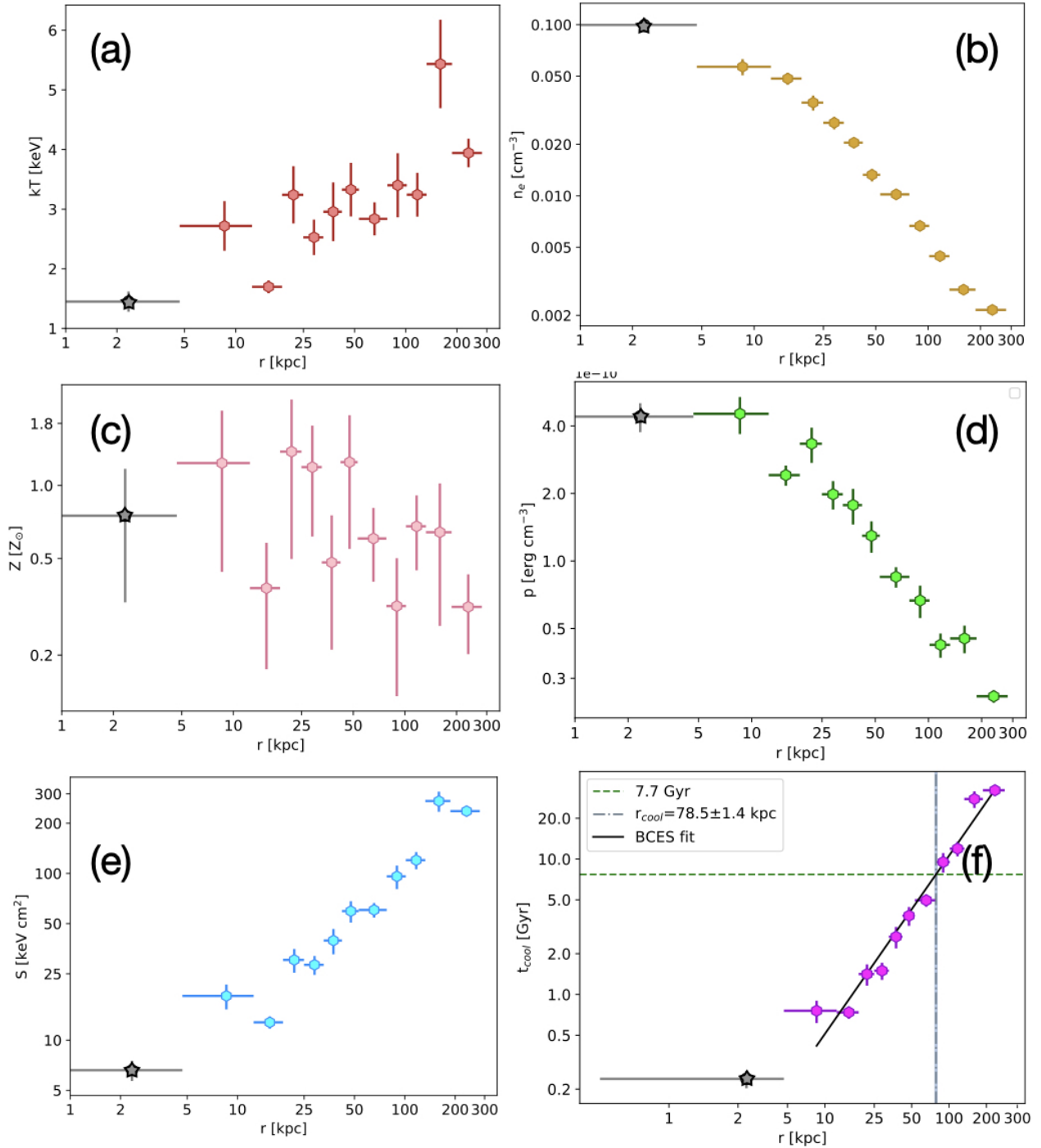
Fig. 3. Circles: deprojected thermodynamic profiles of the ICM in ZwCl 235 between 3″–180″ (for details on the spectral extraction and fitting see Sect. 4.2); star: the innermost gray point in each plot is obtained from the spectral analysis of the inner 3″ of the cluster (for details see Sect. 4.6). *Panel a*: temperature profile. *Panel b*: electron density profile. *Panel c*: abundances profile. *Panel d*: pressure profile. *Panel e*: entropy profile. *Panel f*: cooling time profile, with the best fit power law over the radial range 3″–180″ overlaid in black, the $t_{cool} = 7.7$ Gyr threshold shown with a green dashed line and the cooling radius shown with a gray line. The fit has been performed using BCES (Akritas & Bershady 1996).

to be $L_{bol}[0.1-100\,\mathrm{keV}] \equiv L_{cool} = (1.0 \pm 0.1) \times 10^{44}\,\mathrm{erg\,s^{-1}}$. We can compare this value with the cooling luminosity of other systems in Table 1. Clusters at the top of the list have $L_{cool} \geq 10^{45}\,\mathrm{erg\,s^{-1}}$ (e.g., Abell 1835, McNamara et al. 2006; Abell 2204, Sanders et al. 2009a), those closer to ZwCl 235 have $L_{cool} \geq 10^{44}\,\mathrm{erg\,s^{-1}}$ (e.g., 2A0335+096, Sanders et al. 2009b), while those at lower Hα luminosity have $L_{cool} \geq 10^{43}\,\mathrm{erg\,s^{-1}}$ (e.g., Abell 1668, Pasini et al. 2021; Abell 2495, Pasini et al.

2019). This trend supports the link between the strength of ICM radiative losses and the amount of multiphase gas at the cluster center (e.g., McDonald et al. 2010; Gaspari et al. 2020).

4.3. Extended sloshing and cold fronts

On large scales, the maps shown in Fig. 4 (upper panels) reveal three bow-like discontinuities in temperature and entropy
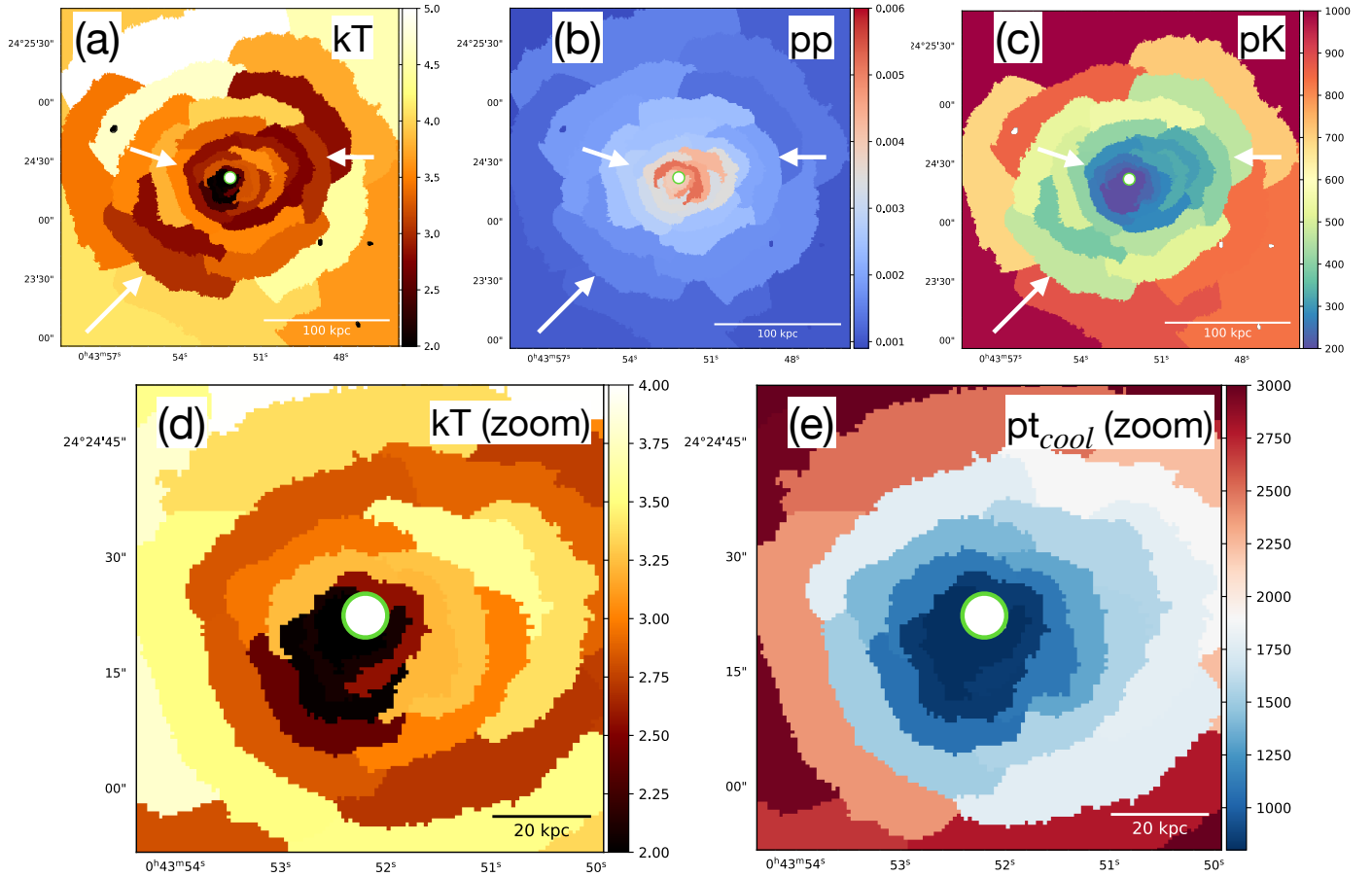
Fig. 4. Spectral maps of the ICM in ZwCl 235 (see Sect. 4.2 for details). *Upper panels*: the temperature (keV), pseudo-pressure (arbitrary units) and pseudo-entropy (arbitrary units) maps are shown. Relative errors are on the order of ~20%. The overlaid white arrows mark the positions of the surface brightness edges discussed in Sect. 4.3. *Lower panels*: the zoomed temperature map (keV) and the pseudo-cooling time map (arbitrary units) show the distribution of the cold gas in the inner ~50 kpc. In all panels, the white-filled, green circle marks the extent of the central X-ray source (see Sect. 4.6).

on opposite sides of the core, which seem nearly continuous in pressure. These properties are usually associated with cold fronts generated by sloshing of the cold ICM. In this context, Bîrzan et al. (2020) first noted the spiral morphology of the ICM and suggested that sloshing could be present in ZwCl 235.

In order to further investigate these features, we created a a Gaussian Gradient Magnitude (GGM) filtered image (see Sanders et al. 2016a) and a residual image. For the first one, we have filtered with the GGM filter the 0.5−7 keV image, using scales of 1, 2, 4, 6, 8 pixels; following the procedure outlined by Sanders et al. (2016b) the resulting five images were combined using a weighted sum. The weights have been set to give smaller scale filters more contribution in the center, and larger scale filters more contribution in the outer regions. The final image is shown in Fig. 5. For the second one, we subtracted the best fit double β model described in the previous section from the original *Chandra* image, obtaining the residual map shown in Fig. 5.

These images highlight an excess to the west of the center, that is spatially connected to the eastern one forming a spiral-like feature. Moreover, we find a possible third edge SE from the core, slightly visible also in the original image. Interestingly, the location of the three edges matches the position of the temperature discontinuities. To measure the magnitude of these jumps, surface brightness profiles were extracted from the 0.5−2 keV band *Chandra* image, using sectors that encompass the disconti-

nuities (see regions overlaid on Fig. 5). The profiles were then fitted with a broken power-law model. The resulting surface brightness profiles and best fit models are shown in Fig. 5 (right panels). We confirmed the presence of an eastern surface brightness edge at $21.6'' \pm 0.3''$ (~34 kpc) from the center, characterized by a density jump of 1.51 ± 0.05, and of a western surface brightness edge at $53.5'' \pm 1.2''$ (~84 kpc) from the center, characterized by a density jump of 1.47 ± 0.05. For the possible SE edge we find a density jump of 1.21 ± 0.12 at $64.0'' \pm 8.5''$ (~100 kpc), but the relatively large uncertainties do not allow us to securely detect it.

To confirm the hypothesis of the cold front nature of the discontinuities, based on the spectral maps, we extracted the spectra of the ICM inside and outside each discontinuity, with a third region extending to the edge of the chip to account for deprojection. Fitting the 0.5−7 keV band spectra with a `projct*tbabs*apec` model returned the deprojected thermodynamic properties (temperature, metallicity, electron density, pressure and entropy) reported in Table 2.

The spectral analysis confirmed that each jump has the typical properties of cold fronts. The ICM temperature inside the east front is lower than outside ($kT_{in}/kT_{out} = 0.65 \pm 0.08$), and we measured a density jump of $n_{e,in}/n_{e,out} = 1.85 \pm 0.17$, and continuous pressure at the interface ($p_{out}/p_{in} = 1.2 \pm 0.2$). For the west front, we found lower ICM temperature ($kT_{in}/kT_{out} = 0.79 \pm 0.11$), higher density ($n_{e,in}/n_{e,out} = 2.39 \pm 0.22$), and
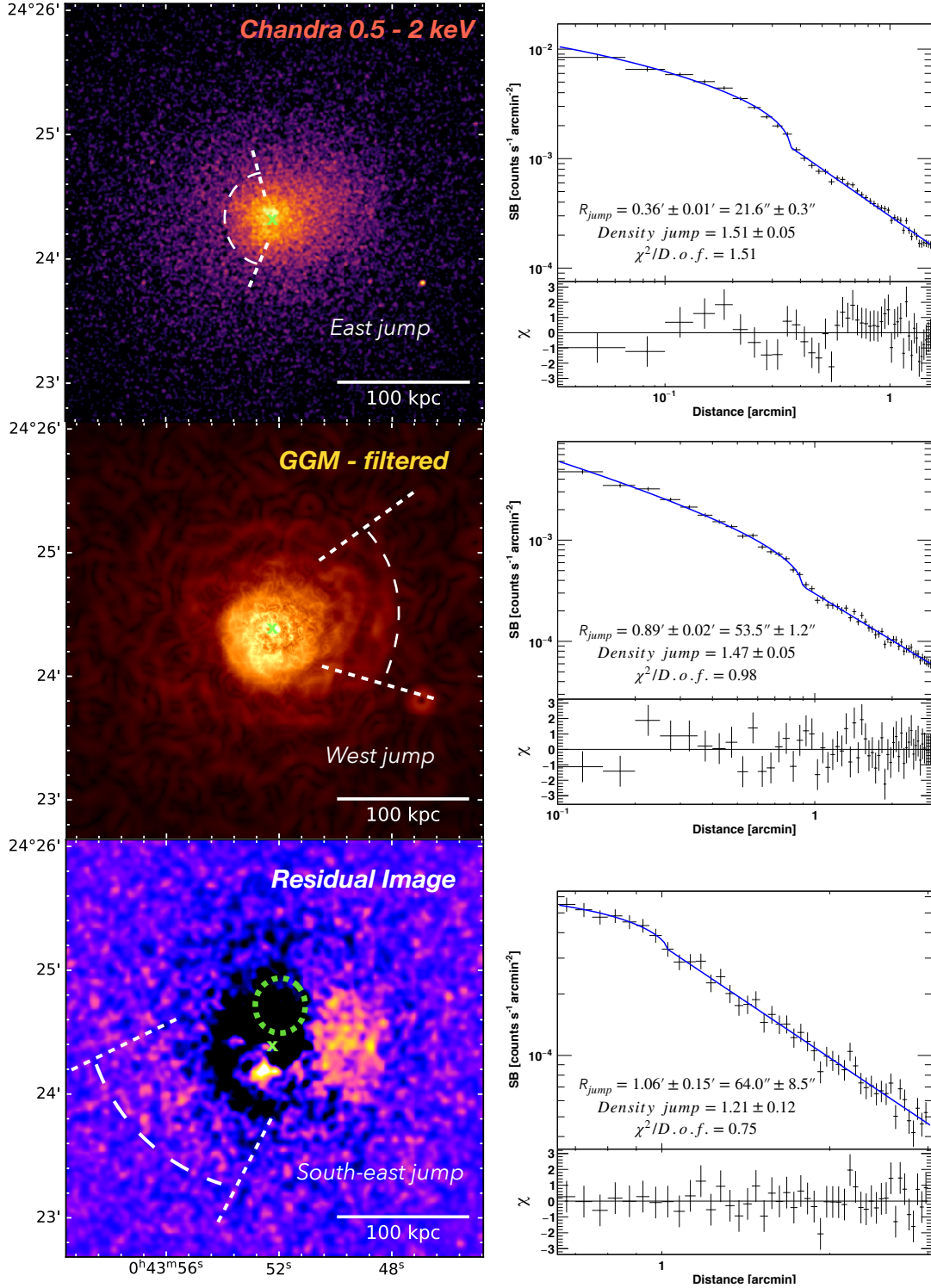
Fig. 5. Surface brightness edges in ZwCl 235. *Left panels*: from top to bottom, 0.5−2 keV band *Chandra* image of ZwCl 235, GGM-filtered image, and double β-model residual image (see Sect. 4.3). White dashed arcs mark the positions of the edges, white dashed lines show the opening angles of the sectors used for the spectral analysis, and the green cross indicates the position of the BCG. In the residual image, the green dashed ellipse indicates the X-ray depression identified by Shin et al. (2016) (see Sect. 4.4). *Right panels*: from top to bottom, surface brightness profiles across the east, west and SE edges. In each panel, the best-fit broken power-law model is overlaid in blue and detailed in the text, while the residuals are shown in the lower boxes.

continuous pressure (p_{out}/p_{in} = 1.7 ± 0.7). For the SE front, we found kT_{in}/kT_{out} = 0.58 ± 0.12, $n_{e,in}/n_{e,out}$ = 2.22 ± 0.19, and p_{out}/p_{in} = 1.3 ± 0.5. Overall, our results support the hypothesis of Bîrzan et al. (2020) that sloshing is shaping the X-ray morphology of ZwCl 235.

Furthermore, we note that the spectral analysis of the cold fronts hints at the inner side having higher abundance than the outer side of the east and the west edges (see Table 2). However, due to the relatively low number of counts, the abundance gradients are marginally significant (~2.2σ for the east front and

Table 2. Spectral analysis of the three surface brightness discontinuities discussed in Sect. 4.3.

Discontinuity	R_i [kpc]	R_o [kpc]	Counts	Z [$Z_\odot$]	kT [keV]	n_e [10^{-3} cm^{-3}]	p_{ICM} [10^{-11} erg cm^{-3}]	K_{ICM} [keV cm^2]
East (34 kpc)	19	34	2436 (99.4%)	$1.01^{+0.29}_{-0.29}$	$2.34^{+0.20}_{-0.21}$	$30.5^{+1.8}_{-1.4}$	$20.9^{+2.1}_{-1.9}$	$23.9^{+2.2}_{-1.6}$
	34	59	2389 (97.9%)	$0.40^{+0.17}_{-0.17}$	$3.56^{+0.28}_{-0.26}$	$16.5^{+0.4}_{-0.4}$	$17.3^{+1.5}_{-1.4}$	$54.8^{+4.4}_{-4.3}$
	59	390	11319 (77.6%)	$0.57^{+0.09}_{-0.10}$	$3.98^{+0.15}_{-0.15}$	$1.7^{+0.1}_{-0.1}$	$2.0^{+0.2}_{-0.2}$	$274.6^{+20.1}_{-20.1}$
West (84 kpc)	47	84	2724 (97.7%)	$0.88^{+0.24}_{-0.24}$	$2.72^{+0.24}_{-0.20}$	$11.3^{+0.4}_{-0.4}$	$9.0^{+0.7}_{-0.8}$	$53.9^{+4.2}_{-4.2}$
	84	142	2249 (92.5%)	$0.41^{+0.28}_{-0.29}$	$3.43^{+0.51}_{-0.45}$	$4.6^{+0.2}_{-0.2}$	$4.9^{+0.7}_{-0.7}$	$123.5^{+16.7}_{-16.7}$
	142	265	2833 (81.1%)	$0.37^{+0.17}_{-0.18}$	$4.12^{+0.33}_{-0.30}$	$2.5^{+0.1}_{-0.1}$	$3.0^{+0.2}_{-0.3}$	$224.9^{+18.5}_{-21.3}$
Southeast (100 kpc)	59	100	1429 (96.3%)	<0.43	$2.45^{+0.34}_{-0.34}$	$8.7^{+0.4}_{-0.4}$	$6.2^{+0.9}_{-0.9}$	$58.0^{+8.3}_{-8.3}$
	100	172	1565 (89.9%)	<0.85	$4.20^{+0.45}_{-0.44}$	$3.9^{+0.2}_{-0.2}$	$4.8^{+0.6}_{-0.6}$	$168.5^{+18.6}_{-18.6}$
	172	515	2454 (54.9%)	$0.51^{+0.25}_{-0.33}$	$4.33^{+0.51}_{-0.50}$	$0.9^{+0.1}_{-0.1}$	$1.2^{+0.1}_{-0.1}$	$459.7^{+54.7}_{-45.6}$

Notes. (1) Name of the discontinuity and distance from the center; (2) and (3) inner and outer radius of the sector used for the spectral analysis (the first sector encloses the front, the second sector contains the region outside the front, and the third, outermost sector is used for deprojection); (4) net photon counts (fraction with regard to the total counts); (5) abundance; (6) temperature; (7) electron density; (8) pressure of the ICM; (9) entropy of the ICM. The χ^2/d.o.f. is 407.8/383 (1.07) for the east front, 231.5/252 (0.92) for the west front and 196.2/243 (0.81) for the SE front.
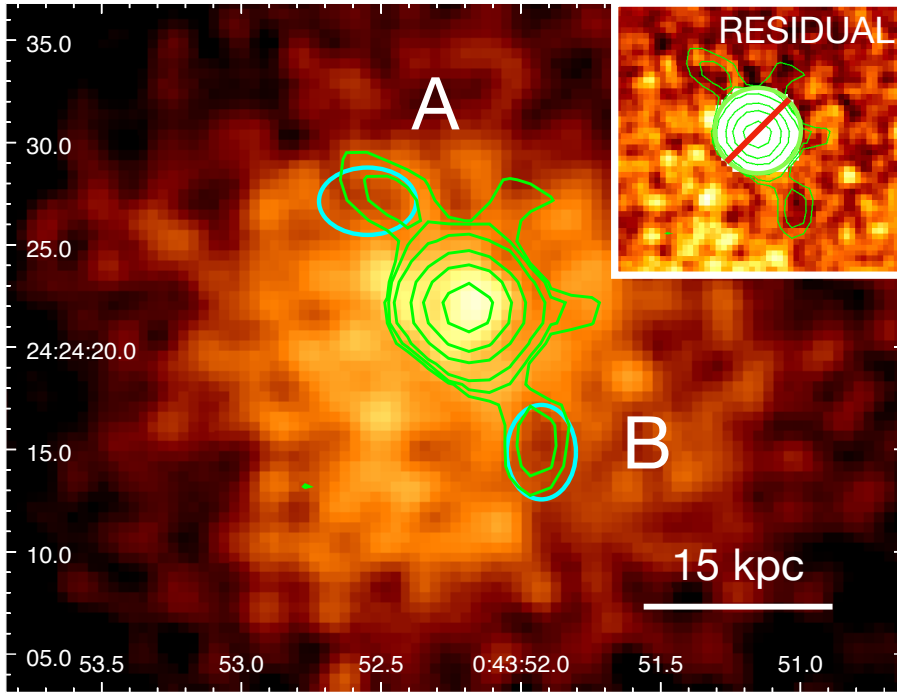
Fig. 6. X-ray depressions in the ICM. *Main panel*: *Chandra* image (0.5−7 keV) of the galaxy cluster core, smoothed with a Gaussian of kernel size 1.5″. The overlaid green contours represent the emission of the central radio galaxy at 3 GHz (same as in Fig. 1), while the cyan ellipses show the position of the putative X-ray cavities discussed in Sect. 4.4. *Upper zoom-in*: double β-model residual image (see Sect. 4.3), showing depressions at the position of the NE–SW radio lobes (contours match those of the *main panel*). The white barred central region is caused by the excision of the inner 3″ from the image during fitting.

~1.4σ for the west front), and for the SE front the metallicity cannot be constrained. Nonetheless, the presence of higher metallicity inside the cold fronts would be consistent with the sloshing scenario (see e.g., Ghizzardi et al. 2013). As the cold, enriched central gas oscillates around the center, it comes at contact with the hotter and less abundant outer ICM, thus generating not only temperature and density, but also abundance gradients. While this is only hinted at in ZwCl 235, enhanced metallicity along low temperature spirals are common (e.g., among the systems in Table 1, the cluster 2A0335+096 shows a low temperature, high metallicity swirl wrapped around the core, Sanders et al. 2009b).

4.4. Evidence for AGN feedback in ZwCl 235

In their systematic search of cavities on a large cluster sample, Shin et al. (2016) found a depression in the residual image of

ZwCl 235, located approximately 14 kpc northwest (NW) of the center, that was tentatively classified as an AGN-inflated X-ray cavity. On the other hand, from the LOFAR observation of the radio galaxy at the center of ZwCl 235, Bîrzan et al. (2020) noted that the 144 MHz lobes are orthogonal to the X-ray cavity identified by Shin et al. (2016), thus questioning its classification. Our aim is to get a closer, dedicated look at the activity of the AGN in ZwCl 235. In this section we investigate the properties and morphology of the central radio galaxy, and we search for imprints of feedback (mainly in the form of X-ray cavities) in the innermost region of the cluster.

Figure 6 shows the VLASS 3 GHz radio contours of the radio galaxy at the center of ZwCl 235, superimposed on the *Chandra* 0.5−7 keV image and on the double β-model residual image. Guided by the radio morphology, we found evidence for the presence of two depressions that match the orientation and extension of the 3 GHz radio lobes (see green ellipses in Fig. 6).

The depressions have diameters of 7.5×5.3 kpc, and are located at a distance of ~ 12 kpc from the center. By comparing the surface brightness of the cavities with that of the surrounding ICM at the same distance from the center, we measured a deficit of 20% at a significance of $\sim 2.3\sigma$ (for comparison, we determined that other regions of apparently low surface brightness within ~ 20 kpc from the center represent depressions of at most $\sim 5\%$ w.r.t. the surrounding ICM). While a deeper *Chandra* exposure would be required to securely detect the two features, the comparison with the morphology of the radio galaxy supports their interpretation as real cavities. We list in Table 3 the physical properties of the two depressions.

To compare the depressions we identified with the putative cavity reported in Shin et al. (2016), we consider the relation between the cavity area (a) and distance from the center (D) discussed in their work. Such relation ($\log a = (0.97 \pm 0.02) \log D - 0.15 \pm 0.02$) would predict an area for the cavities in ZwCl 235 identified here of ~ 130 kpc^2. Thus, while within the scatter found in Shin et al. (2016), the putative cavities in ZwCl 235 are smaller than expected, having an observed area of ~ 32 kpc^2. Nonetheless, even the putative cavity identified by Shin et al. (2016) has a larger area than expected (533 kpc^2). In this respect, considering the residual image of ZwCl 235, we argue that the location of the putative cavity identified by Shin et al. (2016) in their residual image (see green ellipse in Fig. 5) suggests that the depression is a consequence of the sloshing pattern of the ICM of ZwCl 235, rather than an AGN-inflated bubble. Indeed, residual images of sloshing clusters can show negative depressions due to the spiral morphology of the ICM (see e.g., Ueda et al. 2020 for a discussion of such features); in cases where X-ray cavities are also present, the interpretation of the residual patterns requires a detailed analysis (see e.g., the analysis of NGC 1550 in Kolokythas et al. 2020, or of 2A0335+096, Kokotanekov et al. 2018). In the work of Shin et al. (2016), this issue is highlighted for Abell 1991, where a prominent cold front causes over-subtraction of the surface brightness, generating a large depression that resembles a cavity.

In order to determine the history of AGN feedback in this galaxy cluster, we derived the age of the putative cavities combining classical techniques: the sound speed age, the refill time, and the buoyancy age of the cavities (see e.g., Bîrzan et al. 2004). The sound speed age was derived by using the temperature of the ICM at the distance of the cavities from the center ($8''$), measured from the azimuthal profile of Fig. 3. The acceleration at the cavity position ($g \approx 9.8 \times 10^{-8}$ cm s^{-2}), needed to measure the refill and buoyancy ages, was determined from the mass profile of ZwCl 235 obtained by Pulido et al. (2018). From the timescales reported in Table 3, it is clear that the three methods are in good agreement with each other, supporting an average age for the AGN outburst of ≈ 17 Myr. This timescale is consistent with the upper limit of $\lesssim 70$ Myr for the radiative age of the synchrotron emitting particles (see Sect. 4.1).

The mechanical power required to inflate X-ray cavities is typically measured as $4pV/t_{age}$ (e.g., Bîrzan et al. 2004). From the azimuthal pressure profile (see Fig. 3) we determined the pressure p of the ICM at the distance of the cavities from the center. The volume V of the cavities was computed assuming that the depressions can be approximated as oblate ellipsoids (a relative uncertainty of 10% was associated with volumes). For each cavity, the last three rows of Table 3 report the ICM pressure, volume and power (using an average $t_{age} \sim$

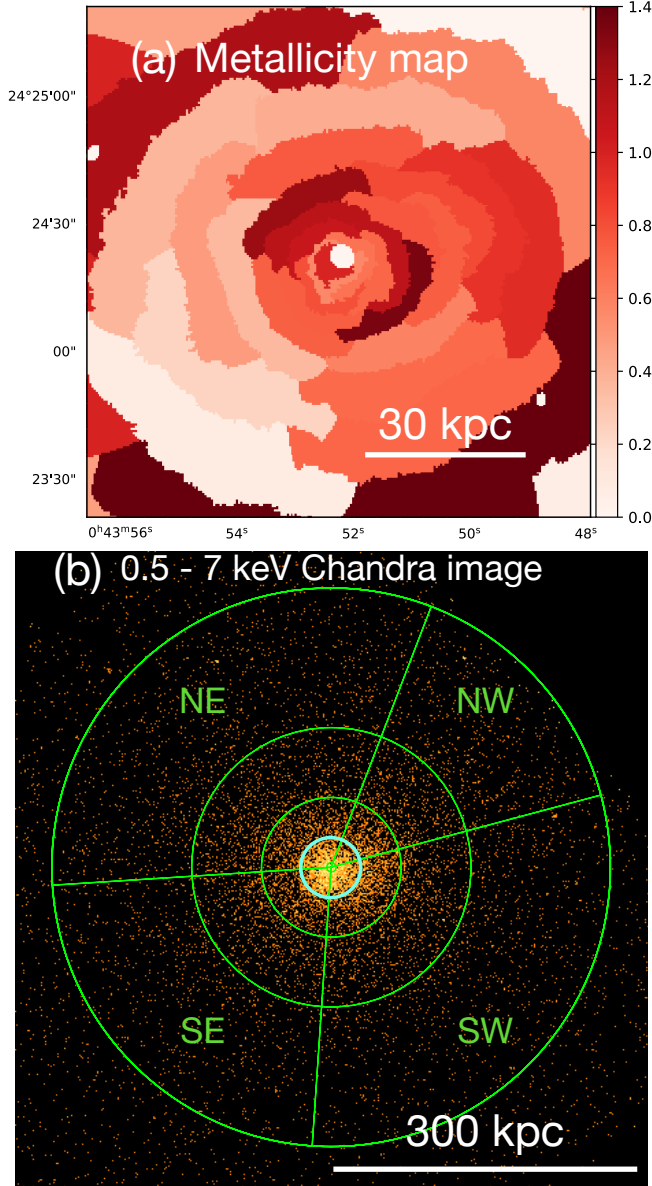**Table 3.** Derived properties of the X-ray depressions discussed in Sect. 4.4 if interpreted as cavities.

	Cavity A	Cavity B
Major semi-axis [kpc]	3.8	3.8
Minor semi-axis [kpc]	2.7	2.7
Distance from the AGN [kpc]	11.5	12.5
Area [kpc^2]	32.2	32.2
Sound speed age [Myr]	15.5 ± 1.8	16.5 ± 1.9
Buoyancy age [Myr]	16.5 ± 1.4	17.6 ± 2.9
Refill age [Myr]	19.9 ± 1.4	19.9 ± 3.1
ICM pressure [10^{-10} erg cm^{-3}]	2.3 ± 0.2	2.3 ± 0.2
Cavity volume [kpc^3]	131 ± 13	131 ± 13
Cavity power [10^{42} erg s^{-1}]	6.0 ± 0.7	6.0 ± 0.7

17 Myr). We measured a total cavity power of $(1.2 \pm 0.2) \times 10^{43}$ erg s^{-1}, which is similar to the cavity power measured in Abell 1668 (Pasini et al. 2021), Abell 2495 (Pasini et al. 2019) and Abell 2052 (Blanton et al. 2011), that are close in Hα luminosity and X-ray flux to ZwCl 235 (see Table 1). Such cavity power is typical of mild AGN outbursts in galaxy clusters, whereas more violent episodes of AGN activity can lead to outburst powers of 10^{45} erg s^{-1} (considering the comparator clusters in Table 1 as e.g., Abell 1835, McNamara et al. 2006, and Abell 2204, Sanders et al. 2009a), up to 10^{46} erg s^{-1} (see e.g., Vantyghem et al. 2014).

4.5. Metallicity of the ICM

By examining the radial profile of metallicity shown in Fig. 3, we do not find evidence for a radial dependence of the abundance in ZwCl 235, that is within the large uncertainties our measurements are consistent with a flat profile. While cool core clusters are known to show central enhancements in iron abundance (e.g., Böhringer et al. 2004b; for instance, this applies to Abell 1068, Wise et al. 2004; Abell 1835, McNamara et al. 2006; or Abell 2204, Sanders et al. 2009a), ZwCl 235 would not be unique in having a flat profile within a few 100 s kpc from the center (see e.g., Abell 1795, Kokotanekov et al. 2018, and Abell 1991, Sharma et al. 2004). The highest metallicity is found in the third bin of the radial profile, that corresponds to the range $12''$–$16''$. Within this radial range, in the map of abundances in ZwCl 235 (shown in Fig. 7, panel a) there are two higher abundance arc-like regions NE and SW of the center, at a distance of $\sim 20''$ (roughly 30 kpc), with a position angle of approximately $132°$. However, given its relatively large error, the metallicity map alone should be used only as a guide to identify interesting features for a further, detailed analysis. To properly investigate metallicity gradients, we then measured the metallicity radial profile in four sectors encompassing the enriched arc-like regions identified by the spectral map (see Fig. 7). The spectrum of each region was fitted with a `tbabs*apec` model; the best-fit metallicity values are shown in Table 4.

With these improved statistics we recover a trend of decreasing metallicity going far from the center for the NE, SE, and SW sectors, as expected in a cool core cluster. Instead, the highest metallicity in the NW sector is found within the second annulus. On the one hand, the uncertainties are still large enough to account for this difference; on the other hand, this could be explained by considering that this region overlaps with the inner side of the west front, for which we found hints of a metallicity

Table 4. Azimuthal and radial variation of metallicity in the ICM (see Sect. 4.5 and Fig. 7, panel b).

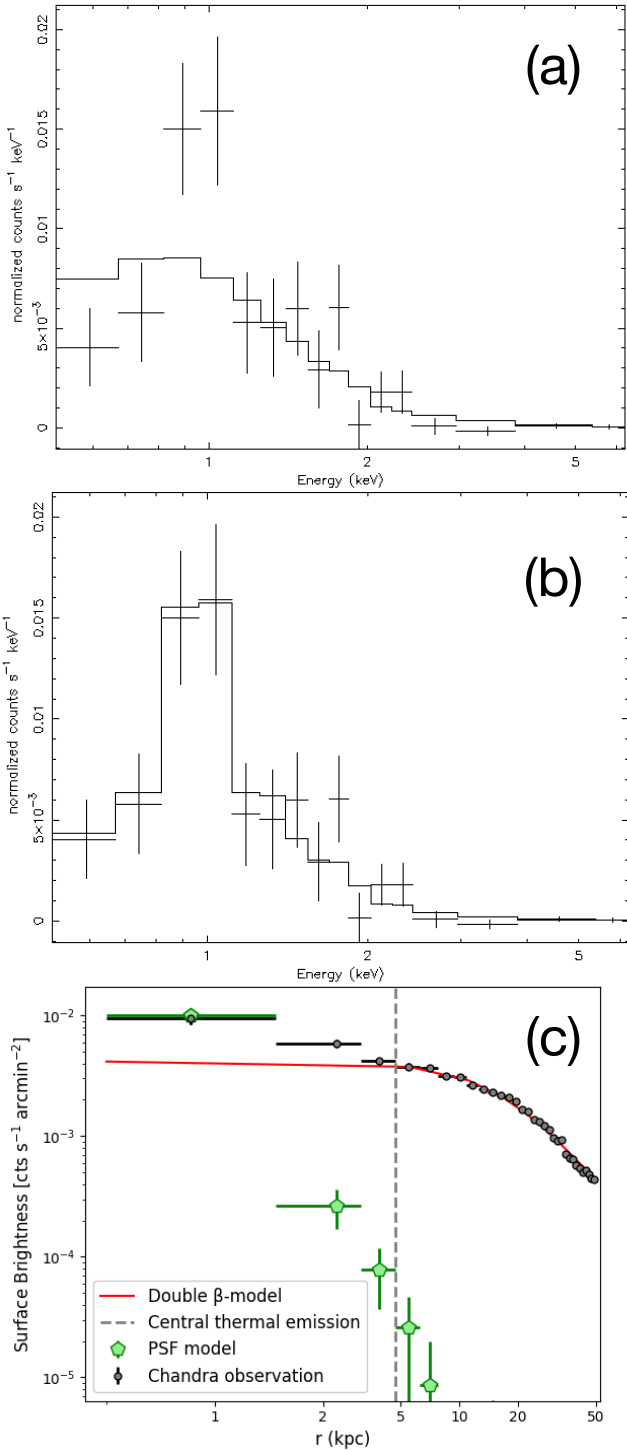| $R_{in}-R_{out}$ [kpc]	Z_{NW} [$Z_\odot$]	Z_{NE} [$Z_\odot$]	Z_{SE} [$Z_\odot$]	Z_{SW} [$Z_\odot$]
4.7–30	$0.58^{+0.29}_{-0.31}$	$1.11^{+0.22}_{-0.20}$	$0.75^{+0.15}_{-0.14}$	$0.99^{+0.17}_{-0.16}$
30–70	$0.72^{+0.24}_{-0.24}$	$0.56^{+0.18}_{-0.17}$	$0.56^{+0.19}_{-0.21}$	$0.81^{+0.16}_{-0.17}$
70–140	$0.53^{+0.25}_{-0.22}$	$0.64^{+0.18}_{-0.19}$	$0.43^{+0.15}_{-0.17}$	$0.57^{+0.18}_{-0.18}$
140–280	$0.31^{+0.24}_{-0.15}$	$0.48^{+0.16}_{-0.14}$	$0.50^{+0.25}_{-0.23}$	$0.33^{+0.12}_{-0.11}$

Notes. (1) Inner and outer radius of the annular sector; (2) abundance in the NW sector; (3) abundance in the NE sector; (4) abundance in the SE sector; (5) abundance in the SW sector. The gray columns highlight the sectors that encompass the metal-rich arcs (see Fig. 7, panel a), which are found in the first radial bin (i.e., within 30 kpc from the center).

arcs are real, we discuss the possible origins of this abundance distribution in Sect. 5.1.

4.6. The nature of the X-ray emission from the inner 3″

The *Chandra* image of Fig. 2 reveals a bright spot in the inner 3″ at the center of the cluster. Considering the VLBA detection of the AGN core (see Sect. 4.1), and the cospatiality of the X-ray bright spot with the radio core as seen at 3 GHz, we need to consider if this X-ray emission is nonthermal. By producing images in different energy bands (0.5−2.0, 2.0−4.0, 4.0−7.0 keV) we verified that the emission fades into the background above 2−3 keV. Thus, if the source is described by a power-law model (emitting nonthermal X-ray radiation), the spectral index could be very steep. Alternatively, the emission could arise from a thermal component with a low (1−2 keV) temperature. To discern between the two models, we extracted the source spectrum from the inner 3″, and we extracted the local background spectrum from an annulus extending from 3″ to 8″ from the center, in order to subtract from the source spectrum the contribution of the surrounding ICM. The spectrum was fit with an absorbed power law (`tbabs*po`), leaving the spectral index Γ and the normalization free to vary. We adopted the *C*-statistics (Cash 1979) to account for the relatively low number of counts (542 counts, including background). The resulting spectral index of $\Gamma = 2.36^{+0.22}_{-0.20}$ is steep (the typical Γ found in BCGs lie in the range 1−2, see e.g., Hlavacek-Larrondo et al. 2013; Yang et al. 2018), as expected from the images produced in different energy bands. The *C*/d.o.f. is 174/151. We verified that the inclusion of an intrinsic absorber (`ztbabs`) is not required.

While this fit constrains quite well the power-law index, there are strong positive residuals (at more than 5σ) in the 0.8−1.0 keV spectral window (see Fig. 8, panel a). According to e.g., Sun et al. (2007), the presence of a soft bump in the X-ray spectrum of brightest cluster galaxies is caused by a thermal emission with temperature of $\approx$1 keV coming from the galactic thermal halo, generating the rise in the region of the Fe-L line. In order to test this hypothesis, we performed a fit of the spectrum with a `tbabs*apec` model, leaving the temperature, abundance and normalization free to vary. We find an improvement in the fit with regard to the power law (*C*/d.o.f. = 153/150) for a thermal plasma with $kT = 1.45^{+0.18}_{-0.15}$ keV and $Z = 0.75^{+0.45}_{-0.40} Z_\odot$. The residuals around 0.8−1.0 keV are accounted for by this model (panel b of Fig. 8). By fitting a combined `tbabs*(apec+po)` model the normalization of the power law

Fig. 7. Metal distribution in the ICM. *Panel a*: metallicity map of ZwCl 235 (see Sect. 4.2 for details on how the map was built), showing two metal rich arcs in the NE–SW direction at roughly 20 kpc from the center. The relative error is ∼30%. *Panel b*: 0.5−7 keV raw *Chandra* image of ZwCl 235. The green sectors correspond to the regions used to study the azimuthal and radial variation of abundances in the ICM (see Sect. 4.5 and Table 4). The metal-rich arcs visible in *panel a* are located within the innermost cyan circle.

gradient. Moreover, within 30 kpc the metallicity is higher along the NE and SW sector, that include the two metal-rich arcs of the metallicity map. The azimuthal gradient is more pronounced with respect to the NW sector, since the opposite SE sector matches the position of the east front. Beyond 30 kpc, the four sectors have similar metallicities.

While the uncertainties prevent us from definitely attesting the existence of metal rich arcs (robust detection of abundance gradients require deep *Chandra* data, see Kirkpatrick & McNamara 2015), the consistent indications from the metallicity map and the study in sectors support the presence of two metal-rich regions between 5−30 kpc from the center, with a position angle of ∼132°. Assuming that the metal-rich

Fig. 8. Analysis of the X-ray emission from the inner 3″. *Panel a*: 0.5−7 keV *Chandra* spectrum of the BCG (black crosses), with the absorbed power-law model (first row of Table 5) over-plotted as a black line. *Panel b*: same as in panel a, with the absorbed thermal model (second row of Table 5) over-plotted as a black line. In both panels, the data are binned to 10 cts bin^{-1} for plotting purposes. *Panel c*: comparison between the 0.5−2 keV surface brightness profile of the PSF (green points) and that of the *Chandra* observation of ZwCl 235 in the inner 50 kpc. The gray dashed line marks the size of the extraction region of the BCG spectrum (3″ ∼ 4.7 kpc; see Sect. 4.6).

approaches zero and the spectral index Γ assumes unphysical values (∼−3), which suggests that the power-law component is

not required. To constrain the contribution of any nonthermal emission, we fixed the power-law index to Γ = 1.9 (following e.g., Russell et al. 2013; Hlavacek-Larrondo et al. 2013), obtaining a 1σ-confidence upper limit on the 2−10 keV flux of the power law of $f_{2-10} \lesssim 2.0 \times 10^{-14}$ erg cm^{-2} s^{-1} (see third row of Table 5). Therefore, we conclude that the X-ray spectrum of the inner 3″ arises mainly from a kernel of ∼1 keV thermal plasma, rather than from an unresolved power law. Deeper X-ray observations might detect nonthermal emission coming from the BCG, which would be expected given the VLBA detection of the AGN and its flat spectral index at GHz frequencies (see also Hogan et al. 2015b).

As a sanity check, we considered the effect of using the blank-sky to model the background, which provided consistent results with those presented here (the details of the blank-sky test are presented in the Appendix A). Considering this, and the fact that the use of a local background is the standard method used to study the X-ray emission from thermal plasma at 1−2 keV in the central kiloparsecs of clusters (see e.g., Sun et al. 2007), we selected the thermal model described in Table 5 as our best-fit model for the central X-ray emission.

Since our analysis suggests that the spectrum within 3″ from the center is likely of thermal origin, the emission should appear extended when compared to the PSF (see e.g., Sun et al. 2007). Using the *Chandra* ray-tracing program ChaRT (Carter et al. 2003) we generated a model of the PSF between 0.5−2.0 keV. Then, we extracted a surface brightness profile of bin width 1″ from the *Chandra* image (in the 0.5−2.0 keV band) and from the PSF model. The profiles are compared in Fig. 8. The surface brightness profile for $r < 3''(\sim5$ kpc) is in excess at more than 5σ with respect to the PSF profile, indicating that the emission is extended. Moreover, the X-ray emission in the inner 5 kpc is also in excess of the double β model describing the ICM surface brightness profile outside this radius (red line in Fig. 8; see Sect. 4.2). Therefore, our analysis unveiled that the bright soft X-ray emission from the inner ≈5 kpc originates from thermal gas at ∼1 keV, whose surface brightness exceeds the expectations from the inward extrapolation of the azimuthally averaged ICM surface brightness profile. Since the source is extended, and the use of a local background removed the contribution of the ICM projected along the line of sight, it is possible to derive the electron density n_e of this thermal component from the normalization of the `apec` component (assuming a volume $V = 4/3\pi r^3$, with $r = 4.7$ kpc). Combining the density and temperature we derived the pressure, entropy and cooling time. We measured $n_e = 0.10 \pm 0.01$ cm^{-3}, $p = 4.4 \pm 0.5 \times 10^{-10}$ erg cm^{-3}, $K = 6.6 \pm 0.8$ keV cm^2 and $t_{cool} = 238 \pm 34$ Myr. To facilitate a comparison with the results on the ICM at $r > 3''$, we include the properties of the thermal gas within 3″ on the plots of Fig. 3 (gray star). As a further validation of these results, we tested fitting the spectrum of the inner 3″ together with the spectra of the annuli between 3″−180″ (see Sect. 4.2) with a `projct*tbabs*apec` model, finding good agreement with the values reported here and shown in the plot of Fig. 3. We observe that the pressure within 4.7 kpc matches that of the surrounding ICM ($p_{ICM} = 4.5 \pm 0.7 \times 10^{-10}$ erg cm^{-3}, see Fig. 3).

Since ZwCl 235 is a cool core cluster (see Sect. 4.2), it could be that this central thermal component represents the coldest, densest phase of the ICM; in particular, cooling of the central gas, which is more efficient at progressively decreasing radii, could be the origin of the 1 keV thermal plasma found on top of the BCG. Indeed, many other galaxy clusters show the cospatiality of soft thermal emission with the region where a nonthermal X-ray point source is found or expected (see e.g.,

Table 5. Spectral analysis of the X-ray spectrum of the BCG using a local background (see Sect. 4.6 for details).

| Model	Γ	$\mathrm{norm_{pl}}$ [ph keV^{-1} cm^{-2} s^{-1}]	kT [keV]	Z [$Z_\odot$]	$\mathrm{norm_{th}}$ [ph keV^{-1} cm^{-2} s^{-1}]	C/d.o.f.
Nonthermal (`tbabs*po`)	$2.36^{+0.22}_{-0.20}$	$1.80^{+0.23}_{-0.22} \times 10^{-5}$	(. . .)	(. . .)	(. . .)	174/151
Thermal (`tbabs*apec`)	(. . .)	(. . .)	$1.45^{+0.18}_{-0.15}$	$0.75^{+0.45}_{-0.40}$	$5.57^{+0.80}_{-0.95} \times 10^{-5}$	153/150
Combined (`tbabs*(apec+po)`)	1.9 (fixed)	$<5 \times 10^{-6}$	$1.40^{+0.19}_{-0.16}$	$0.65^{+0.51}_{-0.43}$	$5.33^{+0.92}_{-0.93} \times 10^{-5}$	155/148

Notes. (1) Model used to fit the spectrum; (2) spectral index of the power law; (3) power-law normalization; (4) temperature of the thermal model; (5) abundance of the thermal model; (6) `apec` normalization; (7) C-statistics/degrees of freedom.

Russell et al. 2013). On the other hand, this central soft component resembles the thermal "coronae" of BCGs discussed in Sun et al. (2007) and Sun (2009), that is X-ray emitting halos of gas surrounding the central elliptical galaxy of the cluster with temperature, entropy, density and cooling time significantly different from those of their ambient ICM (see also Cavagnolo et al. 2009). In this respect, the temperature, entropy, and cooling time of the central thermal component in ZwCl 235 are a factor of ~2, ~3 and ~3 lower than those of the ICM outside 3″, respectively. Additionally, the total gas mass of the 1.4 keV plasma is $\approx 10^9\,M_\odot$, which is in agreement with the mass estimates for BCGs' thermal coronae of Sun et al. (2007). Among the systems listed in Table 1, a thermal corona has been found surrounding the BCG of Abell 2634 (Sun et al. 2007). Considering the above indications, in the following we assume that the 1.4 keV thermal kernel represents the BCG thermal corona. However, we caution that the "coronal" scenario would not indicate the existence of two disconnected gas components at the cluster core (the corona and the ICM) spatially separated by a well-defined boundary. Rather, multitemperature gas phases are likely to coexist in the inner 10 kpc, with the thermal gas at progressively smaller radii being gradually more of stellar origin (see e.g., Brighenti & Mathews 1999). Refining the bin width of radial profiles on scales of, for example, 1″ would reveal if there is actually a smooth decrease in temperature or a sudden drop, but the number of counts in the available *Chandra* data are insufficient.

4.7. The bright X-ray filament

The inspection of the *Chandra* image of ZwCl 235 revealed the presence of a ~20 kpc-long bright filament in the central regions of the ICM (see Sect. 4.2 and Fig. 2). The filament, apparently connected to the central kernel of thermal plasma at 1.4 keV, extends to the south direction along the border of the SW radio lobe. In this section we perform a spectral analysis of the X-ray emission from the filament, with the aim of comparing the spectral properties of the bright feature with those of the surrounding ICM.

In order to properly account for the asymmetrical thermodynamic distribution caused by sloshing, we extracted and fitted the spectrum of four sectors centered on the BCG with inner radius 3″ and outer radius 13″ (see upper panel in Fig. 9). The width of the sectors has been chosen to: (1) encompass the filament (region S1), (2) avoid the cavity region, (3) have two sectors east and west of the nucleus (in order to account for the asymmetry in thermodynamic properties induced by sloshing). Each spectrum was first fit with a one-temperature (1T) model (`tbabs*apec`), with the temperature, normalization and abundance left free to vary. From the resulting values reported in Table 6, it is possible to see that Sector 1 has the lowest temperature; this is consis-
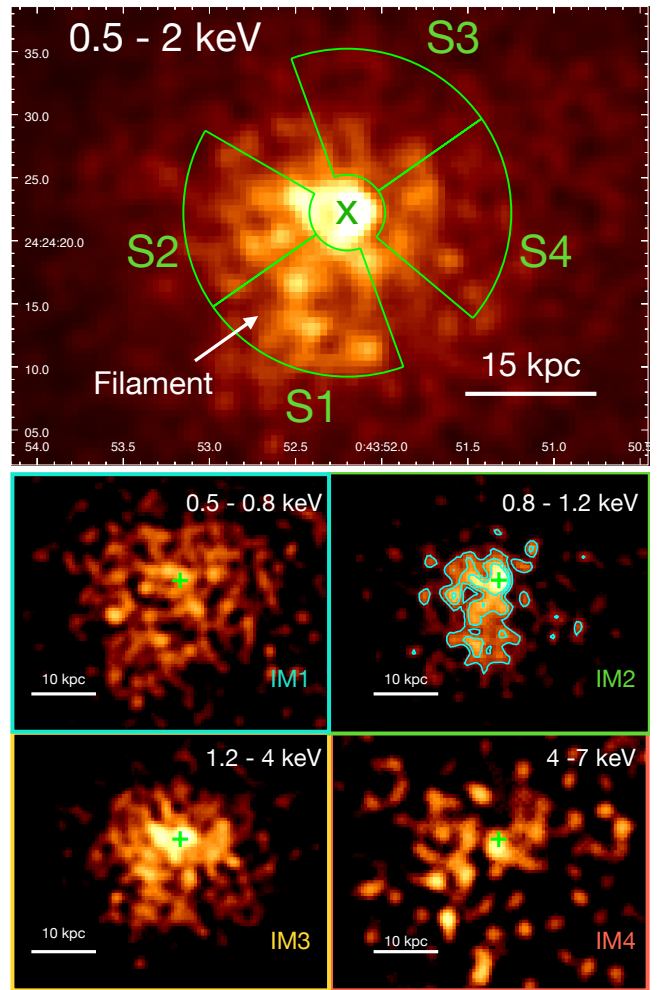
Fig. 9. Different *Chandra* images of the core of the cluster. *Upper panel*: *Chandra* image (0.5–2 keV band) of ZwCl 235, smoothed with a Gaussian of kernel size 1.5″, with the four sectors used to study the properties of the filament, that is encompassed by sector S1, overlaid in green (see Sect. 4.7). The green cross marks the center of the BCG. *Lower panels*: background subtracted, exposure corrected *Chandra* images of the cluster core in different energy bands, used to show that the ~1 keV thermal plasma is found predominantly along the filament. The images are smoothed with a Gaussian of kernel size 1.5″ and have matching color scales. The cyan contours in IM2 are spaced by a factor of $\sqrt{2}$, with the highest being 7×10^{-8} cts s^{-1} cm^{-2}.

tent with the temperature map of Fig. 4, which shows that the minimum in temperature is found along the filament. We note that the χ^2/d.o.f. of the fit to Sector 1 is worse than those of the other sectors. It is possible that a fit with a one-temperature

model does not represent the multiphase nature of the gas. In fact, the X-ray emission from filamentary structures in the cores of clusters has typically been analyzed with a multitemperature approach. Sanders et al. (2009a) used three thermal components at fixed temperatures of 0.5, 1.2 and 4 keV to fit the spectrum of the cold blobs in 2A0335+096. Sharma et al. (2004) detected gas at ~0.8 keV at the center of Abell 1991 by using the surrounding cluster emission as background (thus removing the ambient thermal gas contribution from the cooler emission); moreover, they tested two-temperature models and thermal+cooling flow models to fit the plasma spectrum within ~20 kpc from the center. Similarly, Gitti et al. (2011) used a two-temperature model to describe the emission from the filament in Hydra A. Therefore, we verified whether the inclusion of other components could improve the fit to the filament in ZwCl 235[6].

First, we tested a two-temperature (2T) model (tbabs*(apec+apec)), linking the abundances of the two thermal component. We found that a second thermal model improves the fit (F-statistics value of 4.8, with a p value of 0.01), and suggests the presence of a thermal component with temperature around 1 keV.

We also tested the inclusion of a cooling flow model (tbabs*(apec+mkcflow)), linking the higher temperature and abundances of the mkcflow to those of the apec, freezing the lower temperature to 0.08 keV (the minimum allowed by XSPEC) and leaving the mass deposition rate $\dot{M}$ free to vary. We found that for a $\dot{M} \approx 11\,M_\odot\,\mathrm{yr}^{-1}$ the χ^2/d.o.f. slightly improves, but not significantly.

Thus, the spectrum of the filament is best described by two thermal models, one with $kT_1 \approx 1.3$ keV and the other with $kT_2 \approx 2.7$ keV. We notice the similarity of this fit and the one to the X-ray emission of the BCG. In fact, we found a pronounced bump around 0.8−1.0 keV also in the spectrum of the filament, which is distinctive of a plasma with temperature around 1 keV.

To accurately recover the morphology of the cool component within 20 kpc from the center, it would be necessary to map the temperature of the ICM with a 2T model and a spatial resolution of ~2–3″, which would require a deeper *Chandra* exposure. Here we apply an alternative, approximate method to trace the distribution of the ~1 keV thermal plasma (see also e.g., Massaro et al. 2013; Braito et al. 2017). We produced background subtracted, exposure corrected images of the ICM in four energy bands: 0.5−0.8 keV (IM1), 0.8−1.2 keV (IM2), 1.2−4 keV (IM3), and 4−7 keV (IM4), which are shown in Fig. 9 (lower panels). As it is possible to see, the filament is clearly visible only in IM2, while the other images reveal a relatively spherical or amorphous emission around the X-ray peak (green cross). The contours shown in Fig. 9 start from 3σ above the average surface brightness between 3″−13″ from the center, and nicely trace the region where the bright filament is found.

The presence in a sloshing cluster of a cold filament, with spectral properties that resemble those of the BCG's putative thermal corona, represents an interesting opportunity to investigate how the cycle of AGN feeding and feedback is coupled with the dynamics of the central, low entropy gas. We discuss possible explanation for the properties of the filament in Sect. 5.2.

5. Discussion

In the following, we discuss the results presented in Sect. 4, considering the information on the ICM properties, the BCG X-ray emission and the activity of the central AGN.

---

[6] We tested the inclusion of these components also for the other sectors, finding that either the χ^2/d.o.f. is worse, or the parameters assume nonphysical values.
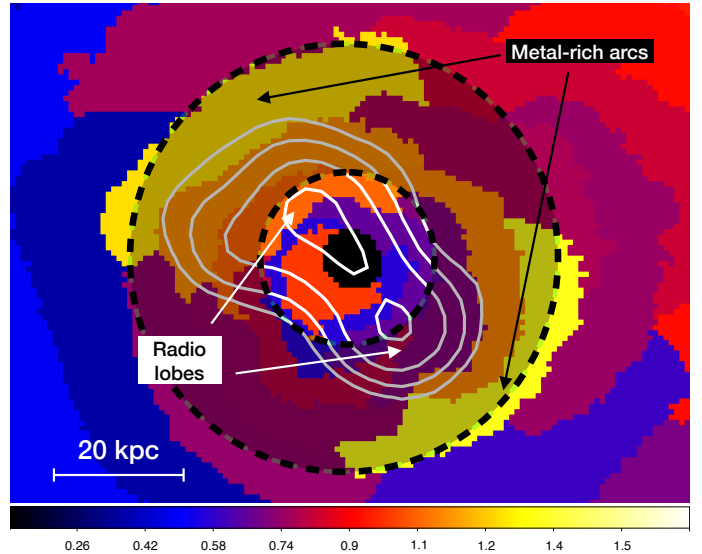
Fig. 10. Zoom-in of the metallicity map shown in Fig. 7. White contours show the central radio galaxy at 144 MHz (levels are the same of Fig. 1). The translucent black area within the black dashed circles shows the predicted location of the iron radius (see text for details), which matches the position of the metal-rich arcs. The black central region corresponds to the BCG, whose X-ray emission was excluded in creating ICM spectral maps (see Sects. 4.2 and 4.6).

5.1. Metal redistribution in the cluster

Our analysis of the ICM metallicity distribution in ZwCl 235 (see Sect. 4.5) unveiled that the metallicity profile shown in Fig. 3 is relatively flat (with a mean $Z \sim 0.9\,Z_\odot$) within ≈ 70 kpc (although it should be noted that the relatively large uncertainties of the profile shown in Fig. 3 prevent us from drawing firm conclusions on the radial trend of abundances). As mentioned in Sect. 4.5, this rather flat profile does not meet the expectations for relaxed clusters, in which the enrichment due to the stellar activity of the BCG has determined a prominent peak in iron abundance (Böhringer et al. 2004b). We note that sloshing may be an efficient mechanism to broaden the distribution of metals in clusters (see e.g., the analysis of Abell 496 in Ghizzardi et al. 2014; see also Roediger et al. 2011; O'Sullivan et al. 2014). Since our analysis indicates that the ICM in ZwCl 235 is sloshing about the center, we may cautiously speculate that an outward transport of metals by the east and west cold fronts could have flattened the metallicity profile within ~70 kpc.

Besides the putative sloshing-induced asymmetries in iron abundance, the metallicity map and our sector-based spectral analysis of the ICM suggest the existence of two high-metallicity arcs on opposite sides of the core, extending out to 30 kpc from the center. These arcs do not seem to be related to the sloshing mechanism, being misaligned by almost 90° with respect to the east and west cold fronts. On the contrary, their position angle of roughly 130° is in good agreement with that of the radio-filled X-ray cavities (~120°, see Sect. 4.4). Additionally, the ~20−30 kpc distance from the center of the two arcs is of the same order as the radio lobe length as seen at 3 GHz (~15 kpc) and at 144 MHz (~20 kpc, see Figs. 1 and 10). Therefore, the presence of excess metallicity in the NE-SW direction may be connected to the inflation of the radio lobes.

Observational evidence of metal transport by AGN mechanical outbursts were first found in the Hydra A cluster (see Simionescu et al. 2009; Kirkpatrick et al. 2009); the subsequent study of other systems (see e.g., Kirkpatrick et al. 2011;

Table 6. Spectral analysis of the ICM in four sectors (first column) within $3''$–$13''$ from the BCG (see Sect. 4.7 and Fig. 9, upper panel for details).

	1T model: `tbabs*apec`			2T model: `tbabs*(apec+apec)`				Cooling model: `tbabs*(apec+mkcflow)`			
	kT [keV]	Z [$Z_\odot$]	χ^2/d.o.f.	kT_1 [keV]	kT_2 [keV]	Z [$Z_\odot$]	χ^2/d.o.f.	kT [keV]	Z [$Z_\odot$]	$\dot{M}$ [$M_\odot$ yr^{-1}]	χ^2/d.o.f.
S1	$2.01^{+0.10}_{-0.17}$	$0.72^{+0.18}_{-0.15}$	51/39	$1.31^{+0.32}_{-0.25}$	$2.66^{+0.97}_{-0.36}$	$0.85^{+0.44}_{-0.32}$	39/37	$2.40^{+0.24}_{-0.42}$	$1.21^{+0.46}_{-0.33}$	$11.4^{+5.5}_{-3.7}$	44/38
S2	$2.24^{+0.22}_{-0.23}$	$0.66^{+0.24}_{-0.21}$	31/32	(...)	(...)	(...)	(...)	(...)	(...)	(...)	(...)
S3	$2.72^{+0.27}_{-0.18}$	$1.08^{+0.44}_{-0.36}$	25/23	(...)	(...)	(...)	(...)	(...)	(...)	(...)	(...)
S4	$3.08^{+0.33}_{-0.32}$	$0.56^{+0.25}_{-0.21}$	28/31	(...)	(...)	(...)	(...)	(...)	(...)	(...)	(...)

Notes. For the 1T model (`tbabs*apec`) we list: (2) temperature; (3) abundance; (4) χ-statistics/degrees of freedom. For the 2T model (`tbabs*(apec+apec)`) we list: (5) temperature of the first component; (6) temperature of the second component; (7) abundance (linked between the two components); (8) χ-statistics/degrees of freedom. For the cooling model (`tbabs*(apec+mkcflow)`) we list: (9) temperature of the `apec` component; (10) abundance (linked between `apec` and `mkcflow`); (11) mass deposition rate; (12) χ-statistics/degrees of freedom.

Kirkpatrick & McNamara 2015) has allowed for a relationship between the cavity power P_{cav} and the altitude of the uplifted gas to be found (the so-called iron radius), R_{Fe}, in the form (see Kirkpatrick & McNamara 2015):

$$R_{Fe\,[kpc]} = (62 \pm 26) \times \left(\frac{P_{cav}}{10^{44}\ erg\ s^{-1}} \right)^{(0.45 \pm 0.06)}. \qquad (9)$$

Using the measured cavity power in ZwCl 235 of 1.2×10^{43} erg s^{-1} (see Sect. 4.4) yields an iron radius of $R_{Fe} = 24.4 \pm 9.9$ kpc. As it is possible to see in Fig. 10, the predicted radial range for the iron radius overlaps with the metal-rich arcs. Altogether, this evidence may suggest that the metal-rich arcs have been generated by uplift of metals in the cluster atmosphere due to the activity of the central AGN (see for comparison the peculiar distribution of metals in e.g., ZwCl 8276, Ettori et al. 2013). However, taking into account the various assumptions on the existence of the metal arcs and the cavities, we caution that these results are more speculative.

5.2. The origin of the cold gas filament

A peculiar feature of the ICM at the center of ZwCl 235 is an arm-like filament, best visible in the soft X-ray band, that extends south of the BCG and is elongated along the southern lobe of the central radio galaxy (see Sect. 4.7). We show in Fig. 11 a multiwavelength view of the central regions of ZwCl 235, with the BCG visible in the optical band (image obtained from the HST archive[7]), the radio galaxy contoured in green and the 0.8–1 keV X-ray emission of the filament contoured in yellow.

We consider three different scenarios that might explain its location, morphology and spectral properties. On the one hand, the filament could represent [i] a cold phase of the ICM, in which cooling has been stimulated due to the activity of the central AGN, that has pushed the gas to an altitude where thermal instabilities might ensue. On the other hand, the gas of the filament could once have been associated with the central gas kernel at 1.4 keV, that may be interpreted as the thermal corona of the BCG (and whose properties are discussed in Sect. 4.6). In this case, the filament could either [ii] represent gas that has been stripped from the BCG due to ram pressure on the corona or [iii] be the result of a small scale *sloshing effect* of the central cool kernel of gas. In the following paragraphs we test and discuss these different hypotheses.

5.2.1. Stimulated cooling

As reported in the introduction, recent observations of cold filamentary gas from X-ray, molecular, and optical data draped around AGN-inflated lobes and cavities have led to hypothesize that AGN feedback can positively stimulate cooling of the ICM. In such theories, the outbursts lifts cold central gas to an altitude where cooling becomes unstable, leading to condensation of small clouds of gas that rain back onto the BCG. There is not a general consensus on the criterion for thermal instabilities to ensue. One the one hand, it has been suggested that unstable cooling occurs within a region where the ratio between cooling time and free fall time reaches a value of ~10–20 (e.g., Voit & Donahue 2015), or less than 70 (Valentini & Brighenti 2015). The free fall time is defined as:

$$t_{ff}(r) = \sqrt{\frac{2r}{g(r)}} \qquad (10)$$

where $g(r)$ is the gravitational acceleration at distance r.

On the other hand, Gaspari et al. (2018) proposed that cooling instabilities are governed by the eddy turnover time t_{eddy}, that is the time at which a turbulent vortex gyrates and produces density fluctuations, and can be defined as:

$$t_{eddy} = 2\pi \frac{r^{2/3} L^{1/3}}{\sigma_v} \qquad (11)$$

where L is the injection scale of turbulence (usually assumed to be described by the diameter of the X-ray cavity), and σ_v is the velocity dispersion of the gas. According to Gaspari et al. (2018), the gas should become multiphase when the ratio between t_{cool} and t_{eddy} is close to unity or lower than one.

Additionally, it has been proposed that cooling is primarily driven by the local values of entropy and cooling time, specifically $K \leq 30$ keV cm^2 and $t_{cool} \leq 1$ Gyr (Cavagnolo et al. 2008). Below these thresholds, which are not related to local dynamical times but only to thermodynamical properties, the presence of multiphase gas and rapid cooling is expected (see e.g., McNamara et al. 2016; Hogan et al. 2017).

We show in Fig. 11 how the positive feedback scenario might apply to ZwCl 235. As it is possible to see, the bright X-ray filament is tangential to southern radio lobe. As discussed in Sect. 4.2, the azimuthal minimum in temperature and entropy is found between $8''$–$12''$ from the center, which corresponds to the projected length of the filament. Additionally, the cooling time map shown in Fig. 4 confirms that t_{cool} drops to the center

---

[7] https://hla.stsci.edu
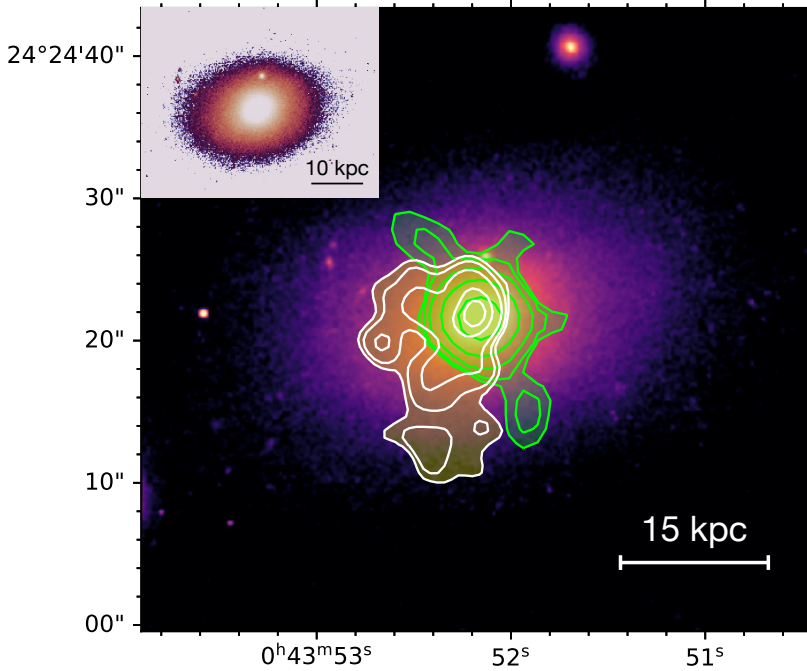
Fig. 11. Multiwavelength view of the BCG in ZwCl 235. *Main panel*: multiwavelength composite image of the center of ZwCl 235. The optical image of the BCG is the *Hubble* Space Telescope image in the broad *V* filter (WFC *F*606*W*). Overlaid in green are filled radio contours at 3 GHz of the central radio galaxy (same as in Fig. 1). Overlaid in yellow are filled X-ray contours between 0.8−1.2 keV (same as in Fig. 9), showing the bulk of the ∼1 keV central thermal plasma (central kernel and bright filament). *Upper left panel*: zoom-in showing the HST optical image of the BCG.

and has its minimum at the position of the filament. We note that the filament appears to be composed of bright clumps (see upper panel in Fig. 9), that might be cold and dense cooling sites. The best fit to the filament X-ray emission (see Sect. 4.7) confirmed that the local ICM is cold, being at a temperature of ∼1.3 keV. With a volume of the cold gas component of 3.2×10^4 kpc^3 and an electron density of ∼0.06 cm^{-3} (see Appendix B), the entropy and cooling time are found to be $K \approx 9.7$ keV cm^2 and $t_{cool} \approx 480$ Myr. We note that these values meet the thresholds of $K \leq 30$ keV cm^2 and $t_{cool} \leq 1$ Gyr for the onset of cooling.

In order to test the t_{cool}/t_{ff} criterion, we computed the free fall time using Eq. (10) and the mass profile of ZwCl 235 (see Sect. 4.4) at the average distance of the filament from the center, that is roughly 12 kpc. With a free fall time of $t_{ff} \cong 29$ Myr, we estimate that $t_{cool}/t_{ff} \sim 17$.

As a last check, we computed the eddy timescale (Eq. (11)) by assuming that the cavity diameter (6.5 kpc) is representative of the injection scale L. We note that the cavity diameter represents a lower limit to the injection scale L, as turbulence could be injected on the whole cold gas region (∼20 kpc). Regarding the velocity dispersion, Gaspari et al. (2018) showed that the different gas phases (hot, warm, neutral and molecular) are linked in terms of σ_v in the inner ∼50 kpc of clusters and groups, with velocity dispersions ranging between 100−200 km s^{-1}. Observationally, this indicates that it is possible to use the condensed gas σ_v as a tracer of the ICM velocity dispersion. By analyzing the kinematics of the molecular gas in a sample of 15 clusters, Olivares et al. (2019) found σ_v in the range 104−196 km s^{-1}. Since ZwCl 235 does not have measurements of the multiphase gas kinematics, we assume $\sigma_v = 200$ km s^{-1}. We note that the assumptions of $L = 6.5$ kpc and $\sigma_v = 200$ km s^{-1} are driven by the aim of being conservative, knowing that larger scales and/or a lower velocity dispersion would determine a longer eddy timescale and a smaller t_{cool}/t_{eddy} ratio. At a distance r of 12 kpc from the center we measure $t_{eddy} \sim 302$ Myr, and thus $t_{cool}/t_{eddy} \sim 480/302 \sim 1.6$, which is close to unity and supports the existence of multiphase gas. Nonetheless, due to the

several assumptions, we consider our measurements of t_{cool}, K and t_{cool}/t_{ff} as our most robust indicators of stimulated cooling.

Overall, we find that ZwCl 235 meets the thermodynamical thresholds and the dynamical criteria. The end product of ICM cooling would be the coexistence of different gas phases over a wide range of temperatures. Probing the presence of such components typically requires either spatially resolved optical line observations (showing extended Hα nebular emission, see e.g., Olivares et al. 2019) or radio observations targeting molecular gas (e.g., ALMA data of CO lines, see e.g., Russell et al. 2019). Such probes are currently unavailable for ZwCl 235, although hints for the existence of multiphase gas in its core can be found in the literature. As reported in the introduction, Crawford et al. (1999) measured a relatively high Hα luminosity of $L_{H\alpha} = (4.1 \pm 0.6) \times 10^{40}$ erg s^{-1}, which could be indicative of extended warm gas nebulae at ∼10^4 K (e.g., Hamer et al. 2016). However, spatially resolved spectroscopy is required to investigate the morphology of the warm gas. Regarding molecular gas, the high resolution optical image in Fig. 11 (upper left panel) does not show evidence for dust lanes in absorption or star forming knots, which indicates that the molecular gas content may not be extreme (for molecular rich clusters see e.g., Abell 1795, Russell et al. 2017, or 2A0335+096, Vantyghem et al. 2016). In this respect, Salomé & Combes (2003) found hints of a CO(1−0) line in the core of ZwCl 235 using an IRAM 30 m observation, and placed an upper limit on the molecular mass of $M_{mol} \leq 2 \times 10^9$ $M_\odot$. It is interesting to note that the test of fitting the filament's spectrum with a cooling model (see Table 6) returned a nonnull value for the mass deposition rate of $\dot{M} \approx 11$ $M_\odot$ yr^{-1}. Interpreting this as an upper limit to the star formation rate, the $M_{mol} \leq 2 \times 10^9$ $M_\odot$ estimated by Salomé & Combes (2003) would be depleted in ≳200 Myr, which is typical of other BCGs surrounded by multiphase gas (see e.g., Molendi et al. 2016; Russell et al. 2016; Castignani et al. 2020; Vantyghem et al. 2021).

Overall, we expect more sensitive optical and radio observations to be able to detect and resolve extended molecular gas, and test the hypothesis that the X-ray filament is undergoing condensation into cold gas clouds.

5.2.2. Ram pressure stripping

Through the process of ram pressure stripping, the ICM can be efficient in removing the hot coronal component of ellipticals, generating X-ray emitting tails behind the galaxy. While the process is most evident in the case of star-forming galaxies (the so-called jellyfish galaxies, see e.g., Poggianti et al. 2017; Boselli et al. 2022), even elliptical galaxies moving in clusters can be subject to extreme stripping of their halos (for a recent example see Mernier et al. 2022). In Sect. 4.7 we noticed the similarity between the spectral properties of the filament ($kT \sim 1.3$ keV, $Z \sim 0.9\,Z_\odot$) and those of the BCG thermal halo ($kT \sim 1.4$ keV, $Z \sim 0.8\,Z_\odot$). As it is possible to see from Figs. 9 and 11, the X-ray emission between $0.8-1.2$ keV shows that the filament is connected to the central source and extends in the south direction. Therefore, it is possible that the gas in the filament originates from the BCG gas halo. In particular, the X-ray tail might have been created in the past after ram pressure stripping of the kernel's outer layers ($\gtrsim 5$ kpc).

It should be noted that the stripping is efficient when galaxies are moving at a relatively high speed with regard to the cluster center; in the case of BCGs, their location at the cluster center indicates that relative motions, if present, are not significant. This applies to ZwCl 235, in which the BCG is coincident with the cluster center. An interesting exception is constituted by the BCG of MKW08 (Tümer et al. 2019), that shows a 40 kpc-long X-ray tail; in this case, however, the host cluster is gravitationally interacting with the galaxy group MKW07, suggesting that residual motions might be present. On the other hand, projection effects might be hiding a significant offset between the BCG of ZwCl 235 and the cluster center, which would imply the presence of relative motions aligned with the line of sight. These motions would then generate the conditions for efficient ram pressure stripping to occur. Nevertheless, if this was the case we would not expect to observe the long X-ray tail (~ 20 kpc), which would be equally projected along the line of sight. Therefore, we argue that a line of sight motion of the BCG is unlikely.

From the observational point of view, if the tail was stripped from the BCG halo we expect millimeter observations to reveal that the molecular gas is still coincident with the central emission. While this information is currently unavailable for ZwCl 235, we can make comparison to the similar clusters reported in Sect. 2. In particular, due to the typically higher densities of molecular gas ($\sim 10^2$ cm^{-3}, e.g., Russell et al. 2019; Ciocan et al. 2021) with regard to those of the hot gas (~ 0.1 cm^{-3}), the cold phase is more difficult to strip and would require relative velocities of ≥ 1000 km s^{-1} (see e.g., Vantyghem et al. 2019). Considering the central position of the BCG, it is very unlikely that it is moving at such supersonic speed (for ZwCl 235 it would imply a Mach number of ~ 2). In this respect, similar conclusions have been drawn for other X-ray bright tails of gas connected to cluster-central BCGs; restricting the comparison to the systems in Table 1, in Abell 1795 (Russell et al. 2017), 2A0335+096 (Vantyghem et al. 2016) and Abell 1991 (Hamer et al. 2012), the cospatiality of the cool ICM and of the molecular gas disfavors the ram pressure stripping scenario, and supports instead a local multiphase condensation of the hot gas.

Observational evidence for the coronal origin of tails can also include higher metallicity along the tail with regard to the ambient gas (see e.g., Tümer et al. 2019). As detailed in Sect. 4.5, the distribution of metals in ZwCl 235 has possibly been perturbed by sloshing and by AGN uplift. This generates significant difficulties in ascribing any metal asymmetry within ~ 15 kpc from the center to other mechanisms such as ram pressure stripping.

While from the metallicity map shown in Fig. 10 there are hints of higher metallicity to the SE side of the BCG, we are unable to further investigate this point due to the short exposure and the overall complex abundance distribution.

5.2.3. Sloshing of the BCG corona

Following gravitational perturbations that offset the densest ICM from the bottom of the potential well of the cluster, the sloshing motion generates spiral patterns in the cold gas distribution. This scenario applies to the ICM in ZwCl 235: the three cold fronts reported in Sect. 4.3 trace the spiral geometry of the gas on scales from 30 kpc (the east front) to 100 kpc (SE front). Here we consider the effect that this perturbation may have had on the cooler, denser plasma at the cluster center. In particular, we investigate the idea that besides generating the three cold fronts in the ICM, sloshing may have shaped the outer layers of the BCG's thermal corona (or the most central ICM phase), leading to the formation of a spiral-tail of gas with $kT \sim 1$ keV.

As already mentioned, the spectral properties of the bright X-ray filament resemble those of the central thermal plasma at 1.4 keV. Furthermore, the cold filament seen in the $0.5-2$ keV image (Fig. 2), the temperature map (Fig. 4) and the $0.8-1.2$ keV contours shown in Fig. 11 is characterized by a hooked morphology: starting from the BCG it heads SE then bends to the south. The arched structures produced by the outward sloshing motion are expected to be over-dense and colder with regard to the surrounding gas, while maintaining pressure equilibrium (McNamara & Nulsen 2007). We showed in Sect. 4.7 that the filament is cold and dense compared to the ambient medium, and we estimate a pressure ratio between the filament and the surrounding ICM (from the profiles of Fig. 3) of ~ 1.1, which supports the pressure equilibrium. Therefore, the filament could represent a small scale (~ 20 kpc in projected length) sloshing tail of gas, that was produced by the same event that has set the oscillating movement of the ICM on tens of kiloparsec scales.

It is possible to provide an estimate of the time taken by the ~ 1 keV gas to slosh to its observed distance from the center. Based on literature examples, there are three methods that can be used to constrain the sloshing timescale:

– Free fall time: if there is no outward pressure to counteract the infall of gas, then the time required for a clump of gas at a distance r to return to the center is given by the free fall time $t_{\rm ff}$. As reported in Sect. 5.2.1, at a distance of 12 kpc the free fall time is $t_{\rm ff} \approx 29$ Myr, which we interpret as a lower limit on the true sloshing timescale (see e.g., Ubertosi et al. 2021).

– Brunt–Väisälä time: recent studies of sloshing clusters have approximated the motion of the gas around the center as an oscillating flow in a stable environment (e.g., Su et al. 2017; Kolokythas et al. 2020; Ubertosi et al. 2021; Pasini et al. 2021), governed by the Brunt–Väisälä timescale (Balbus & Soker 1990):

$$t_{\rm BV}(r) = 2\pi \left(\frac{3g(r)}{5r} \delta_K \right)^{-1/2} \tag{12}$$

where δ_K is the slope of the entropy profile. Since we do not have the statistics to build an entropy profile for the coronal gas, we assume the value of $\delta_K = 2/3$ (see the universal entropy profile discussed in Babyk et al. 2018). For the filament in ZwCl 235 we thus measure $t_{\rm BV} \approx 190$ Myr. As expected from Eq. (12), the Brunt–Väisälä timescale is a factor of roughly 6 longer than the free fall time, and can be considered as an upper limit on the sloshing time.

– Subsonic timescale: the oscillation of gas in sloshing clusters has generally been described as subsonic (Zuhone & Roediger 2016). Assuming that the filament gas has traveled at ~0.5 c_s (see e.g., O'Sullivan et al. 2014; Brienza et al. 2022), its speed would be ~370 km s^{-1} (half the value of the sound speed at the cavity distance from the center, see Sect. 4.4). Thus, it would have taken $\approx$35 Myr to reach a distance of 12 kpc from the center, which is close to the free fall time.

Using the above three methods, we constrain the sloshing timescale for the filament to be between 30−190 Myr. While this range is relatively broad, it is significantly longer than the age of the AGN outburst (~20 Myr), which implies that if the central ~1.4 keV thermal kernel has been subject to sloshing, this happened before the formation of the two cavities.

The sequentiality of the two events opens the possibility that a combination of sloshing and stimulated cooling might explain the filament origin. In particular, a perturbation of the gas might have offset the central thermal gas at ~1.4 keV to the SE of the BCG between 30−190 Myr ago. Considering the volume and electron density of the filament (see Sect. 5.2.1), the total sloshed mass would be ~$2 \times 10^9 \, M_\odot$, that is twice the current mass of the corona. Then approximately 17 Myr ago the AGN started its activity and inflated two bipolar lobes in the NE–SW direction. As the majority of ~1.4 keV gas had already been displaced from the center, the uplift of gas behind the X-ray cavities occurred only where gas to be uplifted was effectively available, that is around the south radio lobe. This argument would explain why the low entropy gas is not found around the north radio lobe. Such a scenario holds for example for 2A0335+096, where the presence of a single filament in the direction of one of the cavities suggests that sloshing may have set a preferred direction for cooling of the ICM (Vantyghem et al. 2016). In Abell 1795, the 40-kpc long cooling wake is likely the result of cooling stimulated by the relative motion of the BCG and the ICM (Crawford et al. 2005; Russell et al. 2017); additionally, in Abell 2052 (that shows signs of sloshing, Blanton et al. 2011) there is a strong asymmetry in the warm gas distribution, with nebular filaments being draped only around the northern inner cavity (Balmaverde et al. 2018). On the contrary, in the case of the Phoenix cluster, for example, the warm gas is draped around both the central X-ray cavities (see McDonald et al. 2015). The inclusion of sloshing can also alleviate the tension between the maximum mass of the gas displaced by the cavity and the actual mass of the 1 keV gas: following Archimedes' principle, a bubble can lift no more mass than the mass it has displaced. From the volume of the cavity reported in Table 3 and the density of the ICM at 12 kpc from the center (~0.04 cm^{-3}), the maximum amount of displaceable gas would be approximately $3 \times 10^8 \, M_\odot$. On the contrary, the mass of the filament is six times higher. Since sloshing can emulate the effect of uplift and provide an alternative way of triggering unstable condensation (see Vantyghem et al. 2019), it is plausible that the cavity expansion is responsible for only a small portion of the uplifted gas. Overall, this scenario provides a consistent explanation for the spectral and morphological properties of the cold filament and its connection to the AGN outburst.

5.3. Cooling and feedback from the cluster to the BCG scales

The X-ray and radio analysis of ZwCl 235 revealed a complex system, where the dynamics of the ICM is strongly coupled with the activity of the central AGN. Besides the sloshing cold fronts, we discovered two radio-filled putative X-ray cavities at ~15 kpc from the BCG, which is surrounded by a thermal halo of gas at ~1.4 keV (cooler than the ambient ICM) and with a radius of ~5 kpc. Starting from this cool kernel, a bright filament of gas (at ~1 keV) extends to the south, parallel to the southern radio lobe (see Fig. 11). In this section we consider how these different features can be interpreted in the context of AGN feeding and feedback mechanisms. Given the different physical scales involved, we refer to the distinction proposed by Gaspari et al. (2020) between the *macro* (10 s–100 s kpc) and *meso* (pc–kpc) scales of AGN feedback.

The radio observations of the central radio galaxy, detailed in Sect. 4.1, reveal that the AGN that inflated the 15 kpc-long radio lobes seen at 3 GHz is currently active: the VLBA image at 5 GHz shows a bright core with bipolar jets emanating in the NE–SW direction. The question we wish to address is which sources of fuel are available for the central SMBH.

Classical pictures of AGN feeding in cool core galaxy clusters predict that cooling of the ICM can provide a resource of cold gas to be accreted by the central engine. In turn, the SMBH launches jets that heat the surrounding medium via cavity inflation and shocks, preventing over-cooling of the ICM and establishing a finely tuned cycle (see Sect. 1). The luminosity of the cooling region, $L_{\rm cool}$, can be used as a proxy for the rate at which cold gas flows to the center and is accreted, $\dot{M}_{\rm cool}$, via the expression:

$$\dot{M}_{\rm cool} = \frac{2}{5} \frac{\mu m_{\rm p}}{kT} L_{\rm cool}. \tag{13}$$

From the properties of the cooling region in ZwCl 235 reported in Sect. 4.2, we estimate a classical cooling rate of $\dot{M}_{\rm cool} = 147 \pm 8.3 \, M_\odot$ yr^{-1}. This is the expected rate of gas cooling in the absence of heating sources. Given the scaling between the cooling luminosity and the Hα luminosity for systems in Table 1 mentioned in Sect. 4.2, and by the definition of $\dot{M}_{\rm cool}$, it is unsurprising to find that systems with lower $L_{\rm H\alpha}$ have mass deposition rates estimated with Eq. (13) of a few tens of $M_\odot$ yr^{-1} (as Abell 2495 and Abell 1668, Pasini et al. 2019, 2021), while more Hα luminous systems have $\dot{M}_{\rm cool} \approx 10^3 \, M_\odot$ yr^{-1} (as Abell 1835, McNamara et al. 2006, or Abell 2204, Sanders et al. 2009a and references therein).

In the presence of central activity, the cavity power is usually assumed to represent a lower limit estimate of the total mechanical power of the AGN. The predictions for the feedback cycle expect the cavity power to be approximately one order of magnitude within the cooling luminosity (or $pV/t_{\rm age} \lessgtr L_{\rm cool} \lessgtr 16pV/t_{\rm age}$, see e.g., Bîrzan et al. 2004; Rafferty et al. 2006; O'Sullivan et al. 2011). This is indeed the case for ZwCl 235, where we estimated $P_{\rm cav} = 4pV/t_{\rm age} = 1.2 \times 10^{43}$ erg s^{-1} and $L_{\rm cool} \approx 10^{44}$ erg s^{-1}, and for the clusters in Table 1 with measurements of both $P_{\rm cav}$ and $L_{\rm cool}$ (namely, Abell 1668, Pasini et al. 2021; Abell 2495, Pasini et al. 2019; Abell 2204, Sanders et al. 2009a; Abell 2052, Abell 1835, 2A0335+096, Abell 478, Abell 2199, Abell 1795, e.g., Rafferty et al. 2006). Therefore, by investigating the feedback cycle on macro scales (between approximately 20−100 kpc), we confirm the coupling of the central radio activity with the thermodynamic properties of the ambient gas, as extensively tested in literature studies (e.g., Böhringer et al. 2004b; Rafferty et al. 2006; Hlavacek-Larrondo et al. 2015).

The above considerations are based on the azimuthally averaged profiles shown in Fig. 3. However, as discussed in Sect. 4.7, the bulk of the coolest gas in ZwCl 235 is not uniformly distributed around the core, as expected from a spherically symmetric inward flow of cold gas. Instead, ~1 keV gas of low entropy ($\leq$30 keV cm^2) and short cooling time ($\leq$0.5 Gyr) is

preferentially found in the south direction, along a bright filament (length of $\approx 20\,\mathrm{kpc}$) that is tangential to the southern radio lobe. As discussed in Sect. 5.2.1, the alignment of the radio galaxy with the lowest entropy medium is likely explained in the context AGN-stimulated condensation of gas in low entropy clouds, with a possible contribution from sloshing (see Sect. 5.2.3). This places ZwCl 235 in good agreement with some well-studied systems in Table 1 (e.g., 2A0335+096 or Abell 1795) where sloshing may have set a preferential direction for AGN-stimulated cooling to occur. According to recent simulations of AGN feeding and feedback (see Gaspari et al. 2018), the cold gas kernels along filaments would ultimately provide an optimal fuel for the central SMBH. Hence, even on smaller scales (between $5-20\,\mathrm{kpc}$) the fueling of the central engine and the growth of the radio galaxy in ZwCl 235 are found to be coupled with the cooling conditions of the ICM.

The observations of AGN activity on meso scales (tens of pc) with the VLBA (see Fig. 1) show that the radio galaxy is active and is currently driving jets through its surroundings. While the study of the macro scales ($20-100\,\mathrm{kpc}$) supports the idea that feeding of the SMBH comes from cooling of the ICM, the BCG thermal halo (see Sect. 4.6) is a further piece of the puzzle. This dense ($n_e \sim 0.1\,\mathrm{cm^{-3}}$) and extended ($\sim 5\,\mathrm{kpc}$ in radius) gas kernel at $1.4\,\mathrm{keV}$ is the gas phase in ZwCl 235 with the lowest entropy ($K \sim 7\,\mathrm{keV\,cm^2}$) and the shortest cooling time ($t_\mathrm{cool} \sim 240\,\mathrm{Myr}$). In the absence of the outer environment, the thermal halo (that we interpreted as the BCG's corona) would thus be the closest source of feeding for the central SMBH. However, the ICM outside $r \sim 5\,\mathrm{kpc}$ in ZwCl 235 seems to be regulating the amount of fuel for the AGN and the resulting energy output. Therefore, it is necessary to understand how the central cool halo of the BCG is coupled with the ICM/AGN feedback cycle. Besides AGN feedback, stellar mass loss and supernovae explosions are likely to contribute to heating of the thermal halo of cluster-central elliptical galaxies (e.g., Sun 2009). The energy injection required from the AGN should be strong enough to reduce cooling without completely destroying the corona. We note that the mechanical AGN power in ZwCl 235 is ~ 20 times larger than the X-ray bolometric luminosity of the corona (see Sects. 4.4 and 4.6). In order for the corona to survive such outburst and be observable, the majority of the AGN mechanical power has likely been deposited outside the BCG ($\geq 5\,\mathrm{kpc}$; see also the discussion in Sun 2009).

We stress that ZwCl 235 differs from the typical systems in the sample of Sun (2009), which comprises coronae of weak cool core clusters ($t_\mathrm{cool} \geq 1\,\mathrm{Gyr}$) and of noncool core clusters; in these objects the $\sim 1\,\mathrm{keV}$ gas halo of the BCG naturally explains how the central AGN is being fueled even though the outer environment is not cooling (see also Tümer et al. 2019). A fitting example is given by Abell 2634 (one of the lowest Hα-luminosity systems listed in Table 1), where the BCG's corona at $1.0\,\mathrm{keV}$ is surrounded by a $\sim 4\,\mathrm{keV}$ ICM (Schindler & Prieto 1997; Sun et al. 2007). In Abell 2634 the corona is the only thermal gas phase with a density, entropy and cooling time that support the existence of cold gas at the cluster core; using the bolometric X-ray luminosity of the 1 keV plasma, Schindler & Prieto (1997) measured a classical mass deposition rate of $\sim 1\,M_\odot\,\mathrm{yr^{-1}}$. On the contrary, ZwCl 235 is a cool core galaxy cluster ($t_\mathrm{cool} \leq 1\,\mathrm{Gyr}$ within the central 25 kpc) that additionally hosts a dense X-ray corona at its center. By applying the standard cooling flow model (Eq. (13)) to the properties of the corona, that has a bolometric luminosity $L_\mathrm{cool}^\mathrm{BCG} = (6.2 \pm 1.3) \times 10^{41}\,\mathrm{erg\,s^{-1}}$ and a temperature of $kT \sim 1.4\,\mathrm{keV}$, we estimate a $\dot{M}_\mathrm{cool} = 1.6 \pm 0.9\,M_\odot\,\mathrm{yr^{-1}}$ (similar to that of the corona in Abell 2634), that is the cool-

ing rate within 5 kpc is about 1% of the ICM cooling rate between 5 kpc and $\sim 79\,\mathrm{kpc}$ (the cooling radius of ZwCl 235, see Sect. 4.2). Thus, the thermal corona is not an "isolated fuel reservoir": both the BCG thermal halo and the central ICM have temperature, entropy and cooling time that may trigger the condensation of $1-2\,\mathrm{keV}$ gas into colder gas clouds. Concerning fueling of the central SMBH, the two components may as well be considered as a single multitemperature gas, with the coldest phase of the ICM being indistinguishable from the corona outer layers.

Overall, we conclude that both the ICM and the thermal halo of the BCG are sources of multiphase, condensed gas in the inner $\sim 20\,\mathrm{kpc}$ of the cluster, with the ICM likely building the larger reservoir.

6. Conclusions

In this article we investigated the AGN feeding and feedback cycle in the galaxy cluster ZwCl 235 using available X-ray (*Chandra*) and radio (LOFAR, VLA, and VLBA) observations of the central radio galaxy. Here we summarize our results.

1. The morphological and spectral analysis of the *Chandra* observation unveiled that ZwCl 235 is a cool core galaxy cluster ($t_\mathrm{cool} \leq 1\,\mathrm{Gyr}$ within 25 kpc from the center, cooling radius $r_\mathrm{cool} = 78.5 \pm 1.4\,\mathrm{kpc}$, and cooling luminosity $L_\mathrm{cool} \approx 10^{44}\,\mathrm{erg\,s^{-1}}$) experiencing sloshing of its ICM, which resulted in the formation of three cold fronts wrapped around the center. The central radio galaxy of ZwCl 235 is currently active: a VLBA observation at 5 GHz revealed a bright core and a pair of jets with a projected total length of 20 pc. The jets are aligned with the radio lobes seen at 144 MHz and 3 GHz by the LOFAR and VLASS surveys, respectively, that extend in the NE–SW direction for approximately $15-20\,\mathrm{kpc}$. We found a pair of X-ray cavities in the ICM matching the position of the radio lobes of the central AGN, whose combined mechanical power is approximately $1.2 \times 10^{43}\,\mathrm{erg\,s^{-1}}$.

2. The *Chandra* spectral analysis of the inner $3''$ ($4.7\,\mathrm{kpc}$) revealed that the X-ray emission originates from a kernel of thermal plasma at $\sim 1.4\,\mathrm{keV}$ coincident with the BCG, with the contribution of nonthermal emission being negligible. The plasma has a density of $\sim 0.1\,\mathrm{cm^{-3}}$ and an entropy of $7\,\mathrm{keV\,cm^2}$, and it is in pressure equilibrium with the surrounding hotter ($\sim 2.7\,\mathrm{keV}$) environment. We interpret this component as the BCG's thermal halo (also known as corona).

3. Our analysis of the metallicity in ZwCl 235 hints at a relatively flat abundance radial profile (with a mean $Z \sim 0.9\,Z_\odot$ within $\sim 70\,\mathrm{kpc}$ from the center) and two enhanced metallicity arc-like regions beyond the AGN radio lobes (extending out to $\sim 30\,\mathrm{kpc}$ from the center). We argue that this distribution of metals may reflect the ICM dynamical perturbations triggered by sloshing and AGN activity. Sloshing may be responsible for an outward transport of metals, traced by the abundance gradients associated with the east and west cold fronts. The central AGN, while inflating the X-ray cavities, possibly generated a pair of metal-rich arcs at 30 kpc from the center in the NE–SW direction by pushing central enriched material to higher altitudes.

4. We discovered that the majority of the cool ICM is found along an X-ray filamentary feature which, starting from the center, extends to the south for approximately 20 kpc. A double thermal model best describes the emission of the filament, with the cooler phase having $kT \sim 1.3\,\mathrm{keV}$,

$n_e \sim 0.06\,\mathrm{cm}^{-3}$, and $t_{cool} \sim 480\,\mathrm{Myr}$. We tested three scenarios for the origin of the filament, namely [i] stimulated cooling by an uplift of cool gas, [ii] ram pressure stripping of the BCG coronal gas, or [iii] sloshing of the BCG thermal halo. By considering the properties of the filament, we conclude that a combination of sloshing and stimulated cooling might provide the best explanation for its origin.

5. By comparing the cooling properties of the X-ray thermal gas (ICM + BCG thermal halo), we have discussed how the cycle of AGN feeding and feedback acts on different scales. Between $20-100\,\mathrm{kpc}$ from the center (macro scales), we confirm standard predictions of the feedback cycle, with the luminosity of the cooling region being related to the mechanical energy released by the AGN outburst. Between $5-20\,\mathrm{kpc}$ from the center (meso-macro scales), the thermodynamic state of the ICM is found to be strongly coupled with radio activity, as demonstrated by the cold filament trailing the southern X-ray cavity. On scales of $\leq 5\,\mathrm{kpc}$ (meso scales), we speculate that the thermal halo of the BCG is contributing to the inflow and cooling of hot gas to lower temperature gas phases, with the ICM building the larger reservoir of fuel for the SMBH.

Therefore, we propose that the AGN is possibly linked with multiple sources of material to be accreted. Future multiwalength follow-up observations may shed light on this galaxy cluster not only by securing the detection of the several features we identified, but also by unveiling the origin of such features.

References

Akritas, M. G., & Bershady, M. A. 1996, ApJ, 470, 706
Allen, S. W., Ettori, S., & Fabian, A. C. 2001, MNRAS, 324, 877
Arnaud, K. A. 1996, in Astronomical Data Analysis Software and Systems V, eds. G. H. Jacoby, & J. Barnes, ASP Conf. Ser., 101, 17
Asplund, M., Grevesse, N., Sauval, A. J., & Scott, P. 2009, ARA&A, 47, 481
Astropy Collaboration (Robitaille, T. P., et al.) 2013, A&A, 558, A33
Astropy Collaboration (Price-Whelan, A. M., et al.) 2018, AJ, 156, 123
Babyk, I. V., McNamara, B. R., Nulsen, P. E. J., et al. 2018, ApJ, 862, 39
Balbus, S. A., & Soker, N. 1990, ApJ, 357, 353
Balmaverde, B., Capetti, A., Marconi, A., & Venturi, G. 2018, A&A, 612, A19
Bharadwaj, V., Reiprich, T. H., Schellenberger, G., et al. 2014, A&A, 572, A46
Bîrzan, L., Rafferty, D. A., McNamara, B. R., Wise, M. W., & Nulsen, P. E. J. 2004, ApJ, 607, 800
Bîrzan, L., Rafferty, D. A., Brüggen, M., et al. 2020, MNRAS, 496, 2613
Blanton, E. L., Randall, S. W., Clarke, T. E., et al. 2011, ApJ, 737, 99
Boehringer, H., Voges, W., Fabian, A. C., Edge, A. C., & Neumann, D. M. 1993, MNRAS, 264, L25
Böhringer, H., Schuecker, P., Guzzo, L., et al. 2004a, A&A, 425, 367
Böhringer, H., Matsushita, K., Churazov, E., Finoguenov, A., & Ikebe, Y. 2004b, A&A, 416, L21
Boselli, A., Fossati, M., & Sun, M. 2022, A&ARv, 30, 3
Braito, V., Reeves, J. N., Bianchi, S., Nardini, E., & Piconcelli, E. 2017, A&A, 600, A135
Brienza, M., Lovisari, L., Rajpurohit, K., et al. 2022, A&A, 661, A92
Brighenti, F., & Mathews, W. G. 1999, ApJ, 512, 65
Brighenti, F., Mathews, W. G., & Temi, P. 2015, ApJ, 802, 118
Carter, C., Karovska, M., Jerius, D., Glotfelty, K., & Beikman, S. 2003, in Astronomical Data Analysis Software and Systems XII, eds. H. E. Payne, R. I. Jedrzejewski, & R. N. Hook, ASP Conf. Ser., 295, 477
Cash, W. 1979, ApJ, 228, 939
Castignani, G., Pandey-Pommier, M., Hamer, S. L., et al. 2020, A&A, 640, A65
Cavagnolo, K. W., Donahue, M., Voit, G. M., & Sun, M. 2008, ApJ, 683, L107
Cavagnolo, K. W., Donahue, M., Voit, G. M., & Sun, M. 2009, ApJS, 182, 12
Chen, H., Jones, C., Andrade-Santos, F., ZuHone, J. A., & Li, Z. 2017, ApJ, 838, 38
Churazov, E., Forman, W., Jones, C., & Böhringer, H. 2000, A&A, 356, 788
Ciocan, B. I., Ziegler, B. L., Verdugo, M., et al. 2021, A&A, 649, A23
Combes, F. 2017, Front. Astron. Space Sci., 4, 10
Combes, F. 2018, Proc. IAU, 14, 77
Crawford, C. S., Allen, S. W., Ebeling, H., Edge, A. C., & Fabian, A. C. 1999, MNRAS, 306, 857
Crawford, C. S., Sanders, J. S., & Fabian, A. C. 2005, MNRAS, 361, 17
de Gasperin, F., Intema, H. T., Shimwell, T. W., et al. 2017, Sci. Adv., 3, e1701634
Donahue, M., & Voit, G. M. 2004, in Clusters of Galaxies: Probes of Cosmological Structure and Galaxy Evolution, eds. J. S. Mulchaey, A. Dressler, & A. Oemler, 143
Ebeling, H., Edge, A. C., Bohringer, H., et al. 1998, MNRAS, 301, 881
Eckert, D., Molendi, S., & Paltani, S. 2011, A&A, 526, A79
Eckert, D., Gaspari, M., Gastaldello, F., Le Brun, A. M. C., & O'Sullivan, E. 2021, Universe, 7, 142
Edge, A. C. 2001, MNRAS, 328, 762
Eilek, J. A. 2014, New J. Phys., 16, 045001
Ettori, S., Gastaldello, F., Gitti, M., et al. 2013, A&A, 555, A93
Fabian, A. C. 1994, ARA&A, 32, 277
Fabian, A. C., Sanders, J. S., Ettori, S., et al. 2000, MNRAS, 318, L65
Fruscione, A., McDowell, J. C., Allen, G. E., et al. 2006, in Society of Photo-Optical Instrumentation Engineers (SPIE) Conference Series, eds. D. R. Silva, & R. E. Doxsey, 6270, 62701V
Gaspari, M., & Sądowski, A. 2017, ApJ, 837, 149
Gaspari, M., McDonald, M., Hamer, S. L., et al. 2018, ApJ, 854, 167
Gaspari, M., Tombesi, F., & Cappi, M. 2020, Nat. Astron., 4, 10
Ghizzardi, S., Rossetti, M., & Molendi, S. 2010, A&A, 516, A32
Ghizzardi, S., De Grandi, S., & Molendi, S. 2013, Astron. Nachr., 334, 422
Ghizzardi, S., De Grandi, S., & Molendi, S. 2014, A&A, 570, A117
Gitti, M., Nulsen, P. E. J., David, L. P., McNamara, B. R., & Wise, M. W. 2011, ApJ, 732, 13
Gitti, M., Brighenti, F., & McNamara, B. R. 2012, Adv. Astron., 2012, 950641
Hallman, E. J., Alden, B., Rapetti, D., Datta, A., & Burns, J. O. 2018, ApJ, 859, 44
Hamer, S. L., Edge, A. C., Swinbank, A. M., et al. 2012, MNRAS, 421, 3409
Hamer, S. L., Edge, A. C., Swinbank, A. M., et al. 2016, MNRAS, 460, 1758
Harris, C. R., Millman, K. J., van der Walt, S. J., et al. 2020, Nature, 585, 357
HI4PI Collaboration (Ben Bekhti, N., et al.) 2016, A&A, 594, A116
Hlavacek-Larrondo, J., Fabian, A. C., Edge, A. C., et al. 2013, MNRAS, 431, 1638
Hlavacek-Larrondo, J., McDonald, M., Benson, B. A., et al. 2015, ApJ, 805, 35
Hogan, M. T., Edge, A. C., Geach, J. E., et al. 2015a, MNRAS, 453, 1223
Hogan, M. T., Edge, A. C., Hlavacek-Larrondo, J., et al. 2015b, MNRAS, 453, 1201
Hogan, M. T., McNamara, B. R., Pulido, F. A., et al. 2017, ApJ, 851, 66
Hudson, D. S., Mittal, R., Reiprich, T. H., et al. 2010, A&A, 513, A37
Jones, E., Oliphant, T., Peterson, P., et al. 2001, SciPy: Open Source Scientific Tools for Python, https://www.scipy.org
Kirkpatrick, C. C., & McNamara, B. R. 2015, MNRAS, 452, 4361
Kirkpatrick, C. C., Gitti, M., Cavagnolo, K. W., et al. 2009, ApJ, 707, L69
Kirkpatrick, C. C., McNamara, B. R., & Cavagnolo, K. W. 2011, ApJ, 731, L23
Kokotanekov, G., Wise, M. W., de Vries, M., & Intema, H. T. 2018, A&A, 618, A152

Kolokythas, K., O'Sullivan, E., Giacintucci, S., et al. 2020, MNRAS, 496, 1471

Lacy, M., Baum, S. A., Chandler, C. J., et al. 2020, PASP, 132, 035001

Liuzzo, E., Giovannini, G., Giroletti, M., & Taylor, G. B. 2010, A&A, 516, A1

Markevitch, M., & Vikhlinin, A. 2007, Phys. Rep., 443, 1

Massaro, F., Harris, D. E., Tremblay, G. R., et al. 2013, ApJS, 206, 7

Mazzotta, P., Markevitch, M., Vikhlinin, A., et al. 2001, ApJ, 555, 205

McDonald, M., Veilleux, S., Rupke, D. S. N., & Mushotzky, R. 2010, ApJ, 721, 1262

McDonald, M., McNamara, B. R., van Weeren, R. J., et al. 2015, ApJ, 811, 111

McKinley, B., Tingay, S. J., Gaspari, M., et al. 2022, Nat. Astron., 6, 109

McMullin, J. P., Waters, B., Schiebel, D., Young, W., & Golap, K. 2007, in Astronomical Data Analysis Software and Systems XVI, eds. R. A. Shaw, F. Hill, & D. J. Bell, ASP Conf. Ser., 376, 127

McNamara, B. R., & Nulsen, P. E. J. 2007, ARA&A, 45, 117

McNamara, B. R., & Nulsen, P. E. J. 2012, New J. Phys., 14, 055023

McNamara, B. R., Wise, M., Nulsen, P. E. J., et al. 2000, ApJ, 534, L135

McNamara, B. R., Wise, M. W., & Murray, S. S. 2004, ApJ, 601, 173

McNamara, B. R., Rafferty, D. A., Bîrzan, L., et al. 2006, ApJ, 648, 164

McNamara, B. R., Russell, H. R., Nulsen, P. E. J., et al. 2014, ApJ, 785, 44

McNamara, B. R., Russell, H. R., Nulsen, P. E. J., et al. 2016, ApJ, 830, 79

Mernier, F., Werner, N., Su, Y., et al. 2022, MNRAS, 511, 3159

Mohapatra, R., Jetti, M., Sharma, P., & Federrath, C. 2022, MNRAS, 510, 2327

Mohr, J. J., Mathiesen, B., & Evrard, A. E. 1999, ApJ, 517, 627

Molendi, S., & Pizzolato, F. 2001, ApJ, 560, 194

Molendi, S., Tozzi, P., Gaspari, M., et al. 2016, A&A, 595, A123

Morganti, R. 2017, Front. Astron. Space Sci., 4, 42

Nulsen, P. E. J., Li, Z., Forman, W. R., et al. 2013, ApJ, 775, 117

Olivares, V., Salome, P., Combes, F., et al. 2019, A&A, 631, A22

O'Sullivan, E., Giacintucci, S., David, L. P., et al. 2011, ApJ, 735, 11

O'Sullivan, E., David, L. P., & Vrtilek, J. M. 2014, MNRAS, 437, 730

O'Sullivan, E., Schellenberger, G., Burke, D. J., et al. 2019, MNRAS, 488, 2925

Pasini, T., Gitti, M., Brighenti, F., et al. 2019, ApJ, 885, 111

Pasini, T., Gitti, M., Brighenti, F., et al. 2021, ApJ, 911, 66

Peterson, J. R., & Fabian, A. C. 2006, Phys. Rep., 427, 1

Peterson, J. R., Paerels, F. B. S., Kaastra, J. S., et al. 2001, A&A, 365, L104

Poggianti, B. M., Moretti, A., Gullieuszik, M., et al. 2017, ApJ, 844, 48

Pulido, F. A., McNamara, B. R., Edge, A. C., et al. 2018, ApJ, 853, 177

Quillen, A. C., Zufelt, N., Park, J., et al. 2008, ApJS, 176, 39

Rafferty, D. A., McNamara, B. R., Nulsen, P. E. J., & Wise, M. W. 2006, ApJ, 652, 216

Robitaille, T., & Bressert, E. 2012, Astrophysics Source Code Library [record ascl:1208.017]

Roediger, E., Brüggen, M., Simionescu, A., et al. 2011, MNRAS, 413, 2057

Rose, T., Edge, A. C., Combes, F., et al. 2019a, MNRAS, 489, 349

Rose, T., Edge, A. C., Combes, F., et al. 2019b, MNRAS, 485, 229

Russell, H. R., Sanders, J. S., & Fabian, A. C. 2008, MNRAS, 390, 1207

Russell, H. R., McNamara, B. R., Edge, A. C., et al. 2013, MNRAS, 432, 530

Russell, H. R., McNamara, B. R., Fabian, A. C., et al. 2016, MNRAS, 458, 3134

Russell, H. R., McNamara, B. R., Fabian, A. C., et al. 2017, MNRAS, 472, 4024

Russell, H. R., McNamara, B. R., Fabian, A. C., et al. 2019, MNRAS, 490, 3025

Salomé, P., & Combes, F. 2003, A&A, 412, 657

Sanders, J. S. 2006, MNRAS, 371, 829

Sanders, J., & Russell, H. 2016, Astrophysics Source Code Library [record ascl:1610.003]

Sanders, J. S., Fabian, A. C., & Taylor, G. B. 2009a, MNRAS, 393, 71

Sanders, J. S., Fabian, A. C., & Taylor, G. B. 2009b, MNRAS, 396, 1449

Sanders, J. S., Fabian, A. C., Russell, H. R., Walker, S. A., & Blundell, K. M. 2016a, MNRAS, 460, 1898

Sanders, J. S., Fabian, A. C., Taylor, G. B., et al. 2016b, MNRAS, 457, 82

Schindler, S., & Prieto, M. A. 1997, A&A, 327, 37

Sharma, M., McNamara, B. R., Nulsen, P. E. J., et al. 2004, ApJ, 613, 180

Shimwell, T. W., Hardcastle, M. J., Tasse, C., et al. 2022, A&A, 659, A1

Shin, J., Woo, J.-H., & Mulchaey, J. S. 2016, ApJS, 227, 31

Simionescu, A., Werner, N., Böhringer, H., et al. 2009, A&A, 493, 409

Sonkamble, S. S., Vagshette, N. D., Pawar, P. K., & Patil, M. K. 2015, Ap&SS, 359, 21

Su, Y., Nulsen, P. E. J., Kraft, R. P., et al. 2017, ApJ, 851, 69

Sun, M. 2009, ApJ, 704, 1586

Sun, M., Jones, C., Murray, S. S., et al. 2003, ApJ, 587, 619

Sun, M., Jones, C., Forman, W., et al. 2007, ApJ, 657, 197

Sutherland, R. S., & Dopita, M. A. 1993, ApJS, 88, 253

Temi, P., Gaspari, M., Brighenti, F., et al. 2022, ApJ, 928, 150

Tümer, A., Tombesi, F., Bourdin, H., et al. 2019, A&A, 629, A82

Ubertosi, F., Gitti, M., Torresi, E., Brighenti, F., & Grandi, P. 2021, MNRAS, 503, 4627

Ueda, S., Ichinohe, Y., Molnar, S. M., Umetsu, K., & Kitayama, T. 2020, ApJ, 892, 100

Valentini, M., & Brighenti, F. 2015, MNRAS, 448, 1979

van der Walt, S., Colbert, S. C., & Varoquaux, G. 2011, Comput. Sci. Eng., 13, 22

van Haarlem, M. P., Wise, M. W., Gunst, A. W., et al. 2013, A&A, 556, A2

van Moorsel, G., Kemball, A., & Greisen, E. 1996, ASP Conf. Ser., 101, 37

van Weeren, R. J., Intema, H. T., Lal, D. V., et al. 2014, ApJ, 786, L17

Vantyghem, A. N., McNamara, B. R., Russell, H. R., et al. 2014, MNRAS, 442, 3192

Vantyghem, A. N., McNamara, B. R., Russell, H. R., et al. 2016, ApJ, 832, 148

Vantyghem, A. N., McNamara, B. R., Russell, H. R., et al. 2019, ApJ, 870, 57

Vantyghem, A. N., McNamara, B. R., O'Dea, C. P., et al. 2021, ApJ, 910, 53

Voit, G. M., & Donahue, M. 2015, ApJ, 799, L1

Wise, M. W., McNamara, B. R., & Murray, S. S. 2004, ApJ, 601, 184

Yang, H. Y. K., & Reynolds, C. S. 2016, ApJ, 829, 90

Yang, L., Tozzi, P., Yu, H., et al. 2018, ApJ, 859, 65

Zuhone, J. A., & Roediger, E. 2016, J. Plasma Phys., 82, 535820301

ZuHone, J. A., Markevitch, M., Brunetti, G., & Giacintucci, S. 2013, ApJ, 762, 78

Appendix A: Alternative test on the X-ray spectrum of the BCG

In this Appendix we show the results of using the blank-sky event file to model the background for the spectral analysis of the X-ray emission of the BCG in ZwCl 235. We extracted the source and background spectrum from a circle of radius $3''$ centered on the BCG from the *Chandra* observation and the blank-sky event file, respectively. The use of a local background in Sect. 4.6 allowed us to remove the contribution of the thermal ambient gas from the BCG spectrum. In order to account for this component when using the blank-sky event file, we included an additional `apec` component in our fit which is meant to describe the ICM projected in front of the central source. Following the study performed in Sect. 4.6, we considered both a nonthermal and a thermal origin for the X-ray emission.

In the first place, we tried to fit the spectrum with a `tbabs*(po+apec)` model. The power-law spectral index, when left free to vary, assumes unphysical values; thus, we fixed it to 1.9 (as done in Sect. 4.6). From the best-fit values reported in Tab. A.1, we note that the power-law normalization is not constrained, resulting in an upper limit similar to that reported in Tab. 5. Additionally, there are positive residuals around

0.8-1.0 keV similar to those found when using a local background. As a consequence, the residuals were not caused by a poor choice of background, but are rather an intrinsic source component.

In the second place, the spectrum was fit in the 0.5-7 keV band with a `tbabs*(apec+apec)`. The temperatures and normalizations of the two `apec` component were left free to vary, while we linked the abundances of the two `apec` together due to the low statistics. The results are reported in Tab. A.1. We identify the component with $kT = 2.53^{+0.54}_{-0.32}$ keV as the one describing the ambient gas, while the one with $kT = 1.10^{+0.27}_{-0.16}$ keV as the one describing the thermal gas in the inner 5 kpc. The latter temperature is slightly lower than that presented in Sect. 4.6, but fully consistent within 1σ errors. From the normalization of the second `apec` and using a volume $V = 4/3\pi r^3$ with $r = 4.7$ kpc (the first `apec` component removes the contribution of the ICM projected along the line of sight), it is straightforward to obtain the electron density $n_e = 0.06^{+0.02}_{-0.04}$ cm^{-3} (Eq. 2). This corresponds to a pressure $p = 1.68^{+1.6}_{-0.8} \times 10^{-10}$ erg cm^{-3} (Eq. 3), an entropy $K = 7.8^{+4.3}_{-2.2}$ keV cm^2 (Eq. 4), and a cooling time $t_{\rm cool} = 355^{+250}_{-150}$ Myr (Eq. 5), which are all consistent with the values presented in Sect. 4.6 within errors.

Table A.1. Spectral analysis of the X-ray spectrum of the BCG using the blank-sky event file as background.

Model	kT [keV]	Z [$Z_\odot$]	norm [ph keV^{-1} cm^{-2} s^{-1}]	Γ	norm [ph keV^{-1} cm^{-2} s^{-1}]	kT [keV]	norm [ph keV^{-1} cm^{-2} s^{-1}]	C/d.o.f.
Nonthermal	$1.83^{+0.17}_{-0.16}$	$0.95^{+0.28}_{-0.22}$	$1.75^{+0.23}_{-0.22} \times 10^{-4}$	1.9	$< 7.09 \times 10^{-6}$	(...)	(...)	165/148
Thermal	$2.53^{+0.54}_{-0.32}$	$1.44^{+0.73}_{-0.55}$	$1.19^{+0.23}_{-0.24} \times 10^{-4}$	(...)	(...)	$1.10^{+0.27}_{-0.16}$	$1.28^{+1.01}_{-0.91} \times 10^{-5}$	158/148

Notes. (1) model used to fit the spectrum; (2-3-4) temperature, abundance and normalization of the `apec` component that accounts for the ambient gas; (5-6) spectral index and normalization of the power law; (7-8) temperature and normalization of the thermal model; (9) C-statistics/degrees of freedom.

Appendix B: Volume of the filament

In this section we detail the method we employed to measure the volume occupied by the two thermal components found in the bright X-ray filament (see Sect. 4.7). In the following, $V_{\rm tot}$ refers to the total volume of the region used for spectral extraction, while V_1 and V_2 refer to the volumes occupied by the cold and hot phases, respectively. The region used for extracting the X-ray properties of the filament, shown in Fig. 9, consists in an annular sector extending from $r_{\rm in} = 3''$ to $r_{\rm out} = 13''$ from the center and with an opening angle of $75°$. Using a projected thermal model, the normalization returned by the fit is referred to a *projected volume* given by the intersection of the spherical shell with a cylinder defined by the width of the annulus and infinite height. Therefore, the total volume can be defined as follows:

$$V_{\rm tot} = \frac{4}{3}\pi(r_{\rm out}^2 - r_{\rm in}^2)^{3/2} = V_1 + V_2. \tag{B.1}$$

Since the fitting has been performed using a 2T model, it is necessary to know the relative contribution of the two thermal components to the total volume, known as the filling factor $f = V_1/V_2$. Following Gitti et al. (2011), assuming that the two

spectral phases are in pressure equilibrium in the same volume the filling factor can be estimated as

$$f = V_1/V_2 = \frac{norm_1}{norm_2}\left(\frac{kT_1}{kT_2}\right)^2, \tag{B.2}$$

where $norm_i$ and kT_i are the normalization and temperature of the i-th component. By combining Eq. B.1 and B.2 we estimated the volume of the cold gas component reported in Sect. 5.2 using the following expression:

$$V_1 = \left(\frac{f}{1+f}\right)V_{\rm tot}. \tag{B.3}$$

For $norm_1 = 5.7 \times 10^{-5}$, $norm_2 = 2.7 \times 10^{-4}$, $kT_1 = 1.31$ keV and $kT_2 = 2.66$ keV we measure a filling factor $f = 0.051$ and a volume $V_1 = 3.2 \times 10^4$ kpc^3.

For comparison, by approximating the volume of the filament as a cylinder with radius 5 kpc and length 17 kpc (determined from the lowest contour shown in IM2 of Fig. 9), we obtain a very similar volume of $V_1 = 3.4 \times 10^4$ kpc^3.